Chapter 5

Numerical experiments with the split semi-Lagrangian formulation of the quasi-elastic equations

5.1 Introduction

In the previous two Chapters a dynamic kernel for a new, nonhydrostatic meso-scale model was developed. The kernel consists of a split semi-Lagrangian formulation of the quasi-elastic σ coordinate equations on a nonstaggered grid. In this Chapter, numerical simulations of highly nonhydrostatic flow are performed with the new kernel. These are in the form of micro- to meso-scale buoyancy driven flows, in two and three spatial dimensions. There are two main objectives with the numerical tests presented here:

- to demonstrate that important nonhydrostatic processes are described by split semi-Lagrangian formulation of the quasi-elastic σ coordinate equations. However, the study of the nonhydrostatic processes themselves fall beyond the scope of the present study. Still, some interesting flow features are indicated and described, with the view on the future application of the new model to the study of nonhydrostatic circulation systems;
- to investigate the accuracy, stability and efficiency characteristics of the split semi-Lagrangian scheme.

It has become standard procedure to test nonhydrostatic models by performing the so called “bubble convection” and “mountain wave” experiments. In the typical bubble convection tests, an elliptically shaped disturbance in the potential temperature is introduced to an isentropic, hydrostatic and dry atmosphere. The buoyant bubble initiates the formation of a density current, and highly nonhydrostatic and nonlinear flow results. Being of no relevance to the study of bubble convection, the Coriolis effect is neglected in these tests. The present chapter commences by reporting on a large set of two-dimensional bubble convection experiments performed with the split semi-Lagrangian scheme (sections 5.2 and 5.3). The experiments may be devided into cold bubble tests (e.g. Droegemeier and Wilhelmson, 1987; Straka et al., 1993) and warm bubble tests (e.g. Droegemeier, 1985; Mendez-Nunez and Carroll, 1994; Gallus and Rancic, 1996), depending on the nature of the initial potential temperature disturbance. The nonhydrostatic processes simulated in convective bubble experiments require the use of model resolutions as fine as 100 m, in both the horizontal and vertical. Typically, thousands or tens of thousands of time steps are required to complete the simulations. Experiments such as these have therefore traditionally been performed in two spatial dimensions, because of the high computational costs involved. Another advantage of working in two dimensions, is that present-day computers have enough speed and memory so that grid-converged numerical solutions for nonlinear two-dimensional problems can be obtained (see Straka et al., 1993). This facilitates the comparison of results obtained with different equation sets and numerical methods when applied to the same flow problem.

After satisfactory performance of the scheme in two spatial dimensions has been illustrated, three-dimensional bubble convection experiments are performed to illustrate that the three-dimensional version of the scheme also performs well (sections 5.4 and 5.6). However, because of the huge computational costs of three-dimensional simulations, these experiments were performed at lower spatial resolutions. The three-dimensional simulations may be compared to the corresponding two-dimensional tests. No grid-converged solutions of the three-dimensionals flow problems are available in literature, however. In fact, there appear to be no reports in literature on three-dimensional simulations of bubble convection. It may be noted that an interesting new bubble convection experiment was designed to test the performance of the new kernel in three spatial dimensions (see section 5.6). In this experiment, a warm bubble is inserted into an isentropic environment with strong vertical wind-shear. The results obtained show close correspondence to the linear theory of storm-splitting, confirming the suitability of using the split semi-Lagrangian formulation of the quasi-elastic equations to simulate highly nonhydrostatic flow in three spatial dimensions.

The numerical experiments performed are also used to investigate the accuracy, stability and efficiency properties of the split semi-Lagrangian scheme. It is shown that the scheme allows the use of large time-steps (implying large Courant numbers) during the advection step of the solution procedure. This implies a computational advantage over explicit solution procedures applied to the quasi-elastic (or fully-elastic) equations. At high spatial resolution, where small time-steps are needed to accurately represent the gravity-wave processes, a relatively large advection time-step may still be used without compromising the overall accuracy of the scheme. This implies a computational advantage over semi-implicit formulations, where the small time-step needed to accurately represent the gravity-wave processes is also used for the advection step. An important part of the overall computational efficiency of the split semi-Lagrangian procedure, involves solving the elliptic equation (3.81 or 3.86) at each advection time-step. It is shown by a series of numerical tests that the SOR procedure described in Chapter 4 is reasonably efficient to use for this purpose.

The experiments in this section were performed using an Intel Pentim IV 3000 MHz personal computer with 512 Mram, or on even smaller computers. Although quite suitable for two-dimensional tests, the available computing power and memory limited the three-dimensional tests in the present study to relatively low spatial resolutions. For the typical size of domain needed for the three-dimensional bubble convection and mountain wave tests, the best spatial resolution that could be afforded was about 500 m in the horizontal, and about 100 m in the vertical.

5.2 Cold bubble experiments in two spatial dimensions

5.2.1 Design of the cold bubble tests

The experiments in this section are patterned after the two-dimensional cold bubble downburst problem described by Droegemeier and Wilhelmson (1987) and Straka et al. (1993). In an initially dry, at rest and isentropic atmosphere with potential temperature 300 K, an elliptically-shaped initial disturbance is introduced for the temperature:

$$\Delta T_0(x,z) = -15\cos^2(\frac{\pi}{2}r), \tag{5.1}$$

for $r \leq 1$, where, $r^2 = [(x - x_c)/x_t]^2 + [(z - z_c)/z_t]^2$, $x_c = 0$ m, $z_c = 3000$ m, $x_t = 4000$ m and $z_t = 2000$ m.

The integration domain extends over $-20000\,m \leq x \leq 20000\,m$ in the horizontal. The top of the model domain is chosen to be 442 hPa (about 6400 m). The center of the initial disturbance is in the middle of the domain in the x direction, that is, 20 km away from the lateral boundaries. Unless where stated differently, the horizontal resolution used in the following experiments is 100 m, and 65 equally spaced σ levels are used to give a vertical resolution of about 100 m on the average. Cold bubble experiments have been widely used to test the performance of z coordinate nonhydrostatic models (e.g. Straka et al., 1993; Wicker and Skamarock, 2002). Fairly recently, similar experiments were performed using terrain-following pressure-based coordinate models (Gallus and Rancic, 1996; Janjic et al., 2001).

5.2.2 Initialization procedure

For all the bubble convection experiments discussed in this chapter, the initial environment is dry, isentropic and in hydrostatic balance. For such an environment the temperature lapse rate is dry adiabatic, and the temperature T_{env} is specified as a function of geometric height by

$$T_{env} = T_{surf\_env} - \frac{g}{c_p}z. \tag{5.2}$$

Here $T_{surf\_env} = 300\,K$ is the surface temperature of the environment. For model initialization, the environmental temperature and geopotential height are needed at each σ level of the model. The potential temperature of the isentropic environment is defined by

$$\theta_{env} = T_{surf\_env} = T_{env}\left(\frac{p_{surf\_env}}{\sigma p_{s\_env} + p_T}\right)^{R/c_p}. \tag{5.3}$$

Substituting for T_{env} in (5.2) by using (5.3) it may be shown that geometric height of each σ level may be calculated from

$$z = \frac{c_p}{g}T_{surf\_env}\left[1 - \left(\frac{\sigma p_{s\_env} + p_T}{p_{surf\_env}}\right)^{R/c_p}\right]. \tag{5.4}$$

Here $p_{surf\_env} = 1000\,hPa$ is the surface pressure of the hydrostatic environment and $p_{s\_env} = p_{surf\_env} - p_T$. Once z is known from (5.4) at each σ level, the corresponding environmental temperature field may be calculated from (5.2). The initial geopotential distribution is given by $\phi = gz$.

To provide positive or negative buoyancy and initiate a density current, a temperature perturbation ΔT, as specified for each particular set of bubble convection experiments, is added to the temperature field. In some experiments the perturbation is specified in terms of the potential temperature, from which ΔT may be evaluated.

In bubble convection experiments performed in z coordinates with the fully compressible equations, the pressure and density fields need to be adjusted towards the perturbed temperature field to obtain an initial state that avoids the generation of strong shock waves in the first time-steps (Droegemeier, 1985; Mendez-Nunez and Carroll, 1994). This may be achieved by a procedure that involves integrating the hydrostatic equation in the vertical at each grid point, to obtain an initial state that is in perfect hydrostatic balance (see Carroll et al., 1987). For the σ coordinate equations solved in the present paper, a different procedure is followed. Here the natural choice to obtain a balanced initial state is to adjust the geopotential field towards the perturbed temperature field. This is achieved by solving (3.86), or (3.81) for the bubble convection experiments in three spatial dimensions, iteratively for the geopotential ϕ. The right-hand side of (3.81) or (3.86) is determined by the initial state of all the variables, for general applications of this initialization procedure. In the case of the bubble convection experiments, however, the perturbed temperature field is the only initial field with a non-zero forcing effect on the right-hand side of (3.81) or (3.86). Equation (5.4) is used to obtain an initial guess for ϕ in the form $\phi = gz$. This type of initialization procedure, where the geopotential distribution on σ levels is adjusted towards the (observed) initial values of variables on σ levels, is perhaps the most natural choice of initialization for a pressure-based atmospheric model. As an alternative to using (3.86) or (3.81) in order to obtain an balanced initial state, it would be possible to integrate the σ coordinate form of the hydrostatic equation in the vertical, in order to obtain a balanced state in perfect hydrostatic balance. However, since the vertical momentum equation is not used explicitly in the split semi-Lagrangian solution procedure, it seems to be more natural to use (3.86) and (3.81) for the purpose of initialization.

The main effect of the initialization procedure when applied to the convective bubble tests, is that the geopotential field reacts to the temperature profile of a given column of air. For the cold bubble experiments the free surface at the model top $\sigma = 0$, above the center of the bubble after initialization, is lower than the value implied by (5.4), with the opposite being true for the warm bubble experiments. In this way, the constant surface pressure is physically consistent with the temperature and geopotential fields, with the less dense (warmer) columns of air occupying larger volumes than the relatively more dense (colder) columns. Another consequence of the initialization procedure is that the geometric height of the bubble after initialization is slightly different to the value specified originally for a particular temperature perturbation ΔT. The initialization procedure is illustrated in Fig. 5.1. The figure shows the geopotential perturbation from the initial state implied by (5.3), obtained iteratively from the SOR procedure (see Chapter 4), using as criterion of convergence $\epsilon = 10^{-5}$ (Panel a), $\epsilon = 10^{-6}$ (Panel b), $\epsilon = 10^{-6}/5$ (Panel c) and $\epsilon = 10^{-7}$ (Panel d). Clearly, the solution is converged for for $\epsilon = 10^{-6}/5$, but not sufficiently converged for $\epsilon = 10^{-6}$ or smaller. A relaxation factor of $rl = 1.9$ was used in the SOR procedure. With this relaxation factor, 562 iterations are needed to satisfy a convergence criterion of $\epsilon = 10^{-6}/5$. The convergence criterion 10^{-7} is not met, even after 15 000 iterations. By trial and error it was established that for values of rl less than 1.9, more iterations are needed before the convergence criterion $10^{-6}/5$ is met. After the initialization step, a convergence criterion of 10^{-6} was found to be sufficient for convergence during the time-integration of the model. A relatively small amount of iterations are then needed to solve (3.81) or (3.86) during each adjustment step of the split semi-Lagrangian solu-

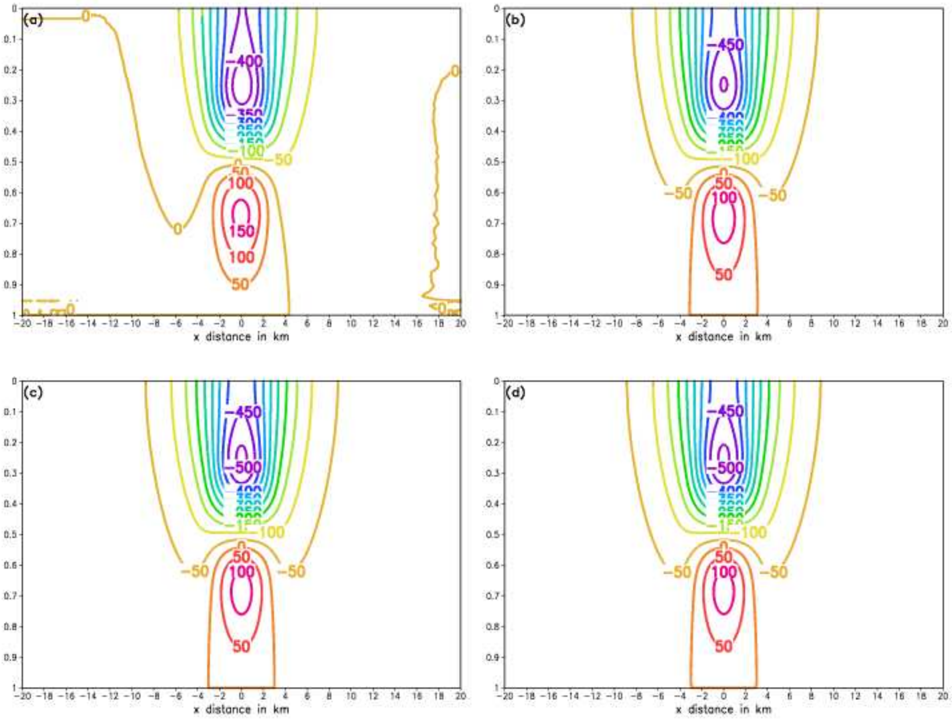

Figure 5.1: Initialization procedure for the two-dimensional cold bubble test. Perturbation from the geopotential distribution corresponding to the hydrostatic, isentropopic environmental state, for $0 \leq \sigma \leq 1$: using as condition of convergence (a) $\epsilon = 10^{-5}$; (b) $\epsilon = 10^{-6}$; (c) $\epsilon = 10^{-6}/5$; (d) 10^{-7}. The contour interval is 50 gpm.

tion procedure (see section 5.2.10).

It should finally be noted that in the practical application of the model to bubble convection experiments, there is no need for an explicit initialization step. The initialization procedure may effectively be carried out at the end of the first adjustment step, when (3.81) or (3.86) is solved for the first time. Since the interpolations involved in the advection step are performed in σ space, there is no need to have the initialized ϕ distribution available in the solution procedure before integrating the horizontal momentum equation(s) during the first adjustment step. Finding the horizontal wind in the first adjustment step from using ϕ as specified by (5.4), instead of using the initialized ϕ distribution, has a negligible effect on the simulations. However, this approach is strictly speaking unphysical, since the geopotential distribution implied by (5.4) belongs to an isentropic, hydrostatic atmosphere, and not to the true initial state that contains the buoyant bubble. Still, this unphysical situation is quickly brought into physical balance, when (3.81) or (3.86) is solved for the first time. In all the experiments reported in this chapter, however, an explicit initialization step was used. This is strictly speaking the correct procedure to apply, since all the fields are in physical balance after initialization. This approach is preferable for more general, real atmosphere applications of the model, for example to initial states that may contain heterogeneous wind fields. In all the experiments performed, the initialization procedure was found to work well, and no strong shock waves are observed to be generated during the first few time-steps of the model.

5.2.3 A reference solution for the cold bubble test

In the reference cold bubble simulation presented here, the D_3 scheme with two-dimensional $(x-\sigma)$ bicubic spatial interpolation is used in the semi-Lagrangian advection step. The spatial derivatives required in the calculation formula for the departure points (x^*, σ^*) (see Chapter 4) are evaluated using centered second order differencing. Centered second order differencing is also used to calculate the quantity $A^*_{p_s}$ and to discretize the spatial derivatives in the adjustment step equations. The advection time-step used is $\Delta t_s = 1\,s$ and the adjustment time-step $\Delta t_a = 0.1\,s$. The Shapiro filter is not used. The values of the diffusion coefficients used in the explicit diffusion step, for diffusion along the x axis, are $K_s = 75\,m^2s^{-1}$ and $K_{Ts} = 75\,m^2s^{-1}$. Diffusion of similar magnitude is applied along the σ axis for u. This is achieved by choosing $K_\sigma = K_s\left(\Delta\sigma^2/\Delta x^2\right)$, so that the non-dimensional quantity $K\Delta t_s/\Delta n^2$ defined in Chapter 4 has the same magnitude along both the x and σ axis (see Janjic et al., 2001). Diffusion of about double the magnitude of that used along the x axis is applied along the σ axis for T, by choosing $K_{T\sigma} = 2K_{Ts}\left(\Delta\sigma^2/\Delta x^2\right)$. These choices of diffusion coefficients were made empirically in order to qualitatively reproduce some quantitative aspects of the reference cold bubble simulation of Straka et al. (1993) (see the discussion later in this section). The diffusion coefficients chosen has an important influence on the time-evolution of the flow (see section

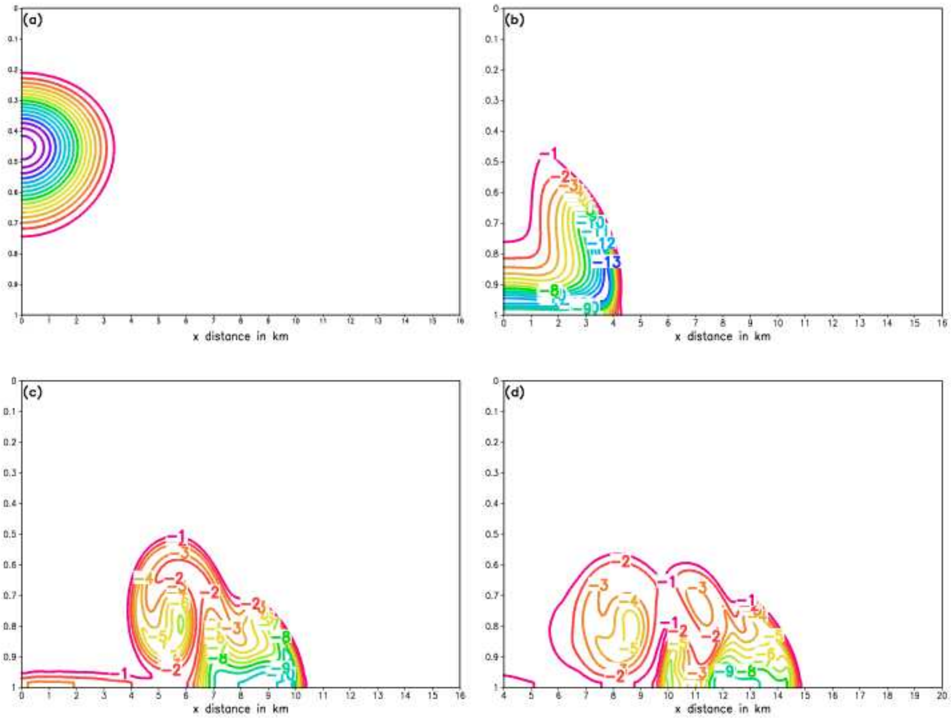

Figure 5.2: Reference solution for the cold bubble test. Potential temperature perturbation in the right-hand part of the integration domain for $0 \leq \sigma \leq 1$: (a) at 0 s; (b) after 300 s; (c) after 600 s; (d) after 900 s. The contour interval is 1 K. Note the displacement of the horizontal scale in (d).

5.2.4). The elliptic equation is solved with SOR, using $rl = 1.9$ as relaxation factor and $\epsilon = 10^{-6}$ as criterion of convergence.

The potential temperature deviations $\theta^{'}$ from the isentropic background state for t = 0, 300, 600 and 900 s are shown in Fig. 5.2, for a simulation with $\Delta t_s = 1\,s$ and $\Delta t_a = 0.1\,s$. The contour interval is 1K. The u component of the wind (upper panel) and the $\hat{w}$ component of the wind (lower panel) after 900 s are shown in Fig. 5.3. The contour interval is 2 ms^{-1}. Recall from Chapter 3 that in the quasi-elastic σ coordinate equations, the relationship $\hat{w} = -\omega RT/gp$ defines the vertical wind. The minimum and maximum of $\theta^{'}$, u and $\hat{w}$ atained for the reference solution (REFC) at t = 900 s are listed in Table 5.1.

In Fig. 5.2 it can be seen that the cold bubble is simulated to descend to the ground. This occurs in conjunction with a downdraft that develops and accelerates, in response to the negative buoyancy associated with the presence

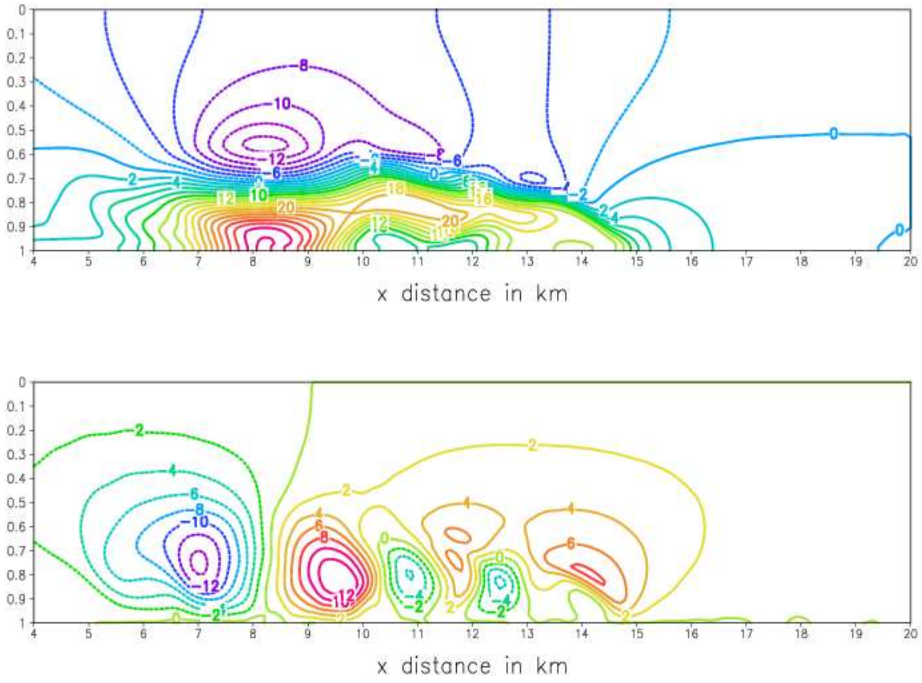

Figure 5.3: Reference solution for the cold bubble test. The u component of the wind (top panel) and the $\hat{w}$ component of the wind (bottom panel) after 900 s in the right-hand part of the integration domain, for $0 \leq \sigma \leq 1$. The contour interval is 2 ms^{-1}.

Table 5.1: Comparison of minimum and maximum values of $\theta^{'}$, u and $\hat{w}$ for the reference solution REFC, and simulations obtained using different values of explicit diffusion (see section 5.2.4). The values of the diffusion coefficients used are $K_s = 75\,m^2s^{-1}$ (REFC and FA), $K_s = 50\,m^2s^{-1}$ (FB), $K_s = 25\,m^2s^{-1}$ (FC) and $K_s = 0\,m^2s^{-1}$ (FD), for diffusion of the u field along the x axis. The diffusion applied along the σ axis, and the T field diffusion, is as specified in the text. Note that diffusion of double the magnitude is applied along the σaxis for T in solution REFC, compared to solution FA.

$Variable$	REFC	FA	FB	FC	FD
$\theta^{'}_{min}$	-9.75	-10.70	-11.19	-11.86	-12.89
$\theta^{'}_{max}$	0.00	0.06	0.10	0.34	1.31
u_{min}	-14.87	-15.73	-17.13	-19.38	-22.24
u_{max}	34.79	31.31	31.64	30.56	31.49
w_{min}	-14.58	-15.58	-16.79	-18.01	-24.32
w_{max}	13.89	17.60	21.51	24.71	29.00

of the cold bubble in the warmer environment. On reaching the surface, the cold air spreads laterally to form a gust front (Panel b). Along the top part of the leading edge of the front, Kelvin Helmholtz shear-instability rotors are formed (Panel c). Three rotors have developed by t = 900 s, and the gust front has progressed to a distance of about 15 km from $x = 0$ (Panel d). The rotors have caused two cold pools to become separated from the main front by t = 900 s (Panel d). Three downdrafts and updrafts exists at t = 900 s in association with the rotors (Fig. 5.3, lower pannel). By this time, the magnitudes of horizontal wind and vertical speed are simulated to peak at 35 ms^{-1} and 15 ms^{-1} respectively (see Table 5.1). The maximum values attained by the horizontal and vertical advection Courant numbers (see Chapter 4) during the full 900 s period are 0.41 and 0.25 respectively. This corresponds to maximum values of 41 ms^{-1} and 23 ms^{-1} attained over the full 900 s period for the magnitudes of u and $\hat{w}$ respectively. Note that equally spaced σ levels are not equally spaced in geometric space, and that this is taken into account during the calculation of the vertical advection Courant number.

The simulation depicted in Figs. 5.2 and 5.3 qualitatively agrees closely with the 25 m resolution grid-converged solution of Straka et al. (1993), and with the (on average) 100 m resolution solutions obtained with three pressure-based models: the fully-elastic nonhydrostatic ETA model (Gallus and Rancic, 1996), the MP-model in σ coordinates (see Gallus and Rancic, 1996), and the fully elastic nonhydrostatic model developed by Janjic et al. (2001). All these models show the the development of three rotors (and therefore the same amount of updrafts and downdrafts) by t = 900 s. The advection time-step $\Delta t_s = 1\,s$ used to obtain the reference solution, is considerably longer than the time steps applied in the previously mentioned studies by other authors, in which Eulerian procedures are used for the advection terms (see section 5.10).

There are only small quantitative differences between the t = 900 s extreme values listed in Table 5.1 for the reference cold bubble solution, and results obtained by other authors using different equation sets and numerical procedures. For example, the maximum horizontal wind speeds at t = 900 s are 36 ms^{-1}, 38 ms^{-1} and 35 ms^{-1} in reference solution of Straka et al. (1993), the nonhydrostatic ETA model and the σ coordinate MP model (Gallus and Rancic, 1996) cold bubble simulations respectively . In the present experiments a value of 35 ms^{-1} is attained (Table 5.1). The minimum vertical wind speeds are respectively about -15ms^{-1}, -14 ms^{-1} and -16 ms^{-1} for the solutions of Straka et al. (1993), and the ETA and MP models respectively, compared to the -15 ms^{-1} obtained in the reference solution (see Table 5.1). Straka et al. (1993) report a minimum potential temperature deviation of -9.77 K for their 25 m resolution simulation, which is in close agreement with the -9.75 K of the reference solution described here. It is shown in section 5.2.4 that the differences in the various simulations may be explained by the different magnitudes of explicit diffusion applied in the various experiments (see also Gallus and Rancic, 1996). In fact, the diffusion coefficients used in the reference solution presented here were empirically selected in order to obtain extreme values of $\theta^{'}$, u, and w at t = 900 s similar to those stated for the reference solution of Straka et al. (1993). It may also be noted that since the cold bubble downburst problem involves dry adiabatic motion, the maximum potential temperature perturbation of 15 K should be conserved during the time-evolution of the flow field. The smaller value that is obtained for $\theta^{'}_{max}$ at t = 900 s, is largely the result of the explicit diffusion and bicubic interpolation applied during the numerical solution procedure.

The gust front in the ETA model simulations progresses to more than 16 km in the x direction in 900 s, compared to 15 km in the present experiment, and about 15.5 km in the test with the σ coordinate MP-model (Gallus and Rancic, 1996) and the 25 m resolution reference solution of Straka et al (1993). Straka et al. report on a large set of cold bubble experiments, performed with different numerical models employing different equation sets and numerical procedures. In these experiments the displacement of the gust front after 900 s in the x direction varies from 14.5 to 17 km. They found that for monotonic schemes the flow features are underdeveloped and move too slowly due to the damping characteristics of these schemes. In the split semi-Lagrangian solution, the phase retardation of short wave- length waves (at advection Courant numbers less than 0.5) by the bicubic interpolation scheme (see Chapter 4) may be responsible for the relatively slightly slower progress of the gust front.

In totality, it may be said that the split semi-Lagrangian scheme with second order differencing gives a quite satisfactory solution of the cold bubble downburst problem. A significant aspect of this result, is that it was obtained without the use of the Shapiro filter. Clearly, the stationary two-grid-interval waves and the generally retarded short wave-length waves on the nonstaggered grid (see Chapter 4) are not having a significant impact on the simulations. This is probably due to the explicit diffusion (smoothing) applied, as well as the strong damping of short wave-lengths during each advection step by the bicubic interpolation scheme (see Chapter 4). Indeed, the reference solution potential temperature deviation field (and wind field) is somewhat diffused in comparison to the results obtained by Straka et al. (1993), Gallus and Rancic (1996) and Janjic et al. (2001). The third rotor is not as strongly developed by 900 s as in the simulations by these authors. In the remaining sections, it is shown how high order spatial differencing and smaller values of the explicit diffusion coefficients, in combination with the Shapiro filter, may be used to improve on the reference solution described in this section.

5.2.4 The effect of explicit diffusion

Different choices of diffusion coefficients may explain the differences in quantitative results obtained by different authors for the cold bubble test (see Gallus and Rancic, 1996). In the experiments in this section, it is illustrated that the choice of diffusion coefficient applied in the cold bubble test indeed has a significant impact on the time evolution and amplitudes of the simulated fields. It may be noted that in the split semi-Lagrangian solution procedure presented in Chapter 4, explicit diffusion is applied (in a split manner) only to the horizontal wind and temperature fields. Since the vertical momentum equation is not used explicitly, diffusion is only applied indirectly to the vertical velocity field $\dot{\sigma}$, when the diffused horizontal wind field is used in the vertical integration of the continuity equation (see Chapter 4).

In order to quantify in some way the effects of explicit diffusion on the simulations, a series of experiments employing different values of the diffusion coefficients were performed. In the four experiments described here, diffusion of the same magnitude is applied to the u and T fields. That is, $K_s = K_{Ts}$, and the diffusion coefficients applied were chosen to be of similar impact along both the x and σ axis. This is achieved by choosing $K_\sigma = K_s\left(\Delta\sigma^2/\Delta x^2\right)$ and $K_{T\sigma} = K_{Ts}\left(\Delta\sigma^2/\Delta x^2\right)$, so that the non-dimensional quantity $K\Delta t_s/\Delta n^2$ defined in Chapter 4 has the same magnitude along both the x and σ axis. Except for the diffferent values of the diffusion coefficients used, the settings of the experiments described in this section are exactly as for the reference simulation described in section 5.2.3. The extreme values at t = 900 s obtained for $\theta^{'}$, u and $\hat{w}$ are listed in Table 5.1 for the different choices of diffusion coefficients $K_s = 75\,m^2s^{-1}$ (FA), $K_s = 50\,m^2s^{-1}$ (FB), $K_s = 25\,m^2s^{-1}$ (FC) and $K_s = 0\,m^2s^{-1}$ (FD) respectively. Fig. 5.4 shows $\theta^{'}$ after 900 s for $K_s = 75\,ms^{-2}$ (Panel a), $K_s = 50\,ms^{-2}$ (Panel b), $K_s = 25\,ms^{-2}$ (Panel c), and $K_s = 0\,ms^{-2}$ (Panel d). The corresponponding $\hat{w}$ fields are shown in Fig. 5.5.

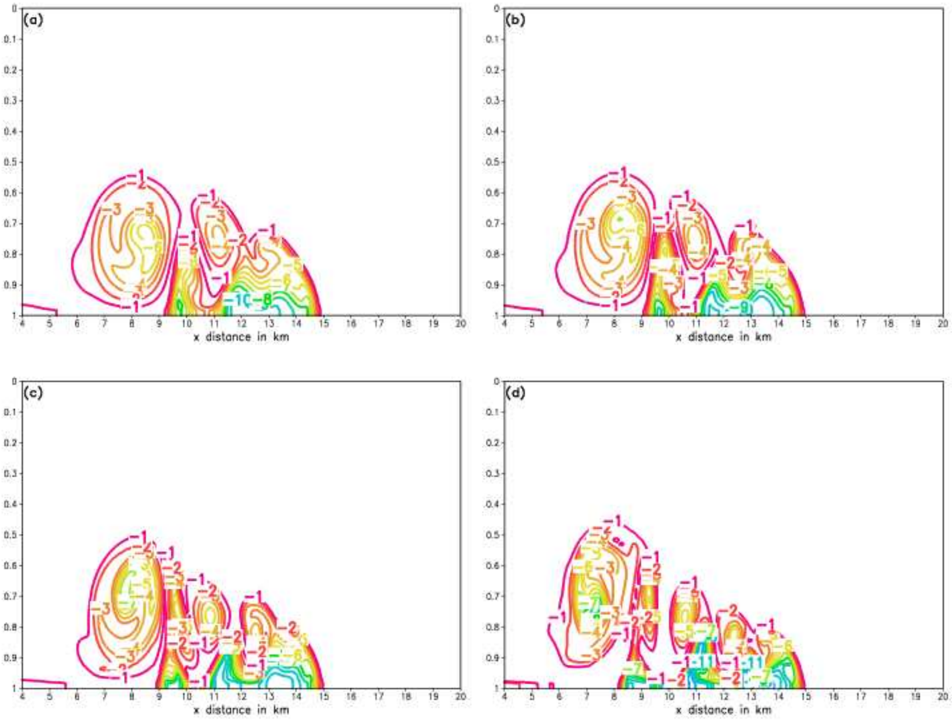

Figure 5.4: The potential temperature deviation after 900 s for the cold bubble test, in the right-hand part of the integration domain, for $0 \leq \sigma \leq 1$: (a) $K_s = 75\, ms^{-2}$; (b) $K_s = 50\, ms^{-2}$; (c) $K_s = 25\, ms^{-2}$; (d) $K_s = 0\, ms^{-2}$. The contour interval is 1K.

The downdraft of the third rotor depicted in Panel a of Fig. 5.3 (obtained with $K_s = 75\, m^2 s^{-1}$), is more intense than in the reference solution (Fig. 5.3, lower panel). The corresponding potential temperature field (Panel a in Fig. 5.4) has reacted to the stronger downdraft , showing the presence of the third rotor more clearly than in the reference solution. In fact, the time evolution of the potential temperature deviation pattern depicted in Panel a of Fig. 5.4, is in very close agreement to the solutions presented by Straka et al. (1993), Gallus and Rancic (1996) and Janjic and Gerrity (2001). In the simulation with $K_s = 50\, m^2 s^{-1}$, the initial stage of the development of a fourth rotor can be seen (note the formation of a fourth updraft in Panel b of Fig. 5.5). In all the experiments with smaller diffusion coefficients, a fourth rotor is well developed by t = 900 s (Panels c and d of Fig. 5.5). The $\theta^{'}$ fields in Panels c and d of Fig. 5.4 show that the third rotor has caused a third cold pool to separate from the main front, with the fourth rotor impacting on the evolution of the $\theta^{'}$ field at the leading edge of the gust front. Another noteworthy feature of the simulations with $K_s = 25\, m^2 s^{-1}$ and $K_s = 0\, m^2 s^{-1}$, is how the first rotor to develop starts to impact on the trailing edge of the gust front. Some of the cold air in this region gets caught in the updraft of the first rotor and is advected upwards (Panels c and d in Fig. 5.4).

Clearly, relatively larger values of the diffusion coefficients slow down the time-evolution of the main flow features. In simulations carried out with $K_s = 75\, m^2 s^{-1}$, $K_s = 50\, m^2 s^{-1}$, and for the reference solution settings, a small perturbation in the potential temperature can be seen at the leading edge of the gust front by t = 900 s. This perturbation is indicative of the initial stages of the development of the fourth rotor, that becomes fully developed after t = 900 s. Straka et al. (1993) report similar behaviour for their 25 m resolution reference solution.

All the simulations, even the one with zero diffusion, remained stable during the 900 s integration period. However, the $\hat{w}$ fields for $K_s = 25\, m^2 s^{-1}$, and in particular for $K_s = 0\, m^2 s^{-1}$, are noisy (Panels c and d of Fig. 5.5). More negative aspects of the simulations with relatively small diffusion coefficients are apparent from Table 5.1. Noting that potential temperature is conserved in an adiabatic atmosphere, the large positive values of $\theta^{'}_{max}$ for small values of the diffusion coefficients (see columns FC and FD in Table 5.1) are indicative of numerical inaccuracy. The errors in $\theta^{'}_{max}$ are diffused when higher values for the diffusion coefficients are used (see columns FA and FB in Table 5.1).

When comparing the extreme values of $\theta^{'}$, u and $\hat{w}$ listed in Table 5.1 for the simulations with various diffusion coefficients, it should be kept in mind that the time-evolution of the various simulations are different. This, and the reduced damping effect of explicit diffusion at smaller diffusion coefficients, may explain the larger extreme values of the vertical wind obtained for smaller diffusion coefficients (Table 5.1). However, the exceptionally large values of $\hat{w}$ obtained

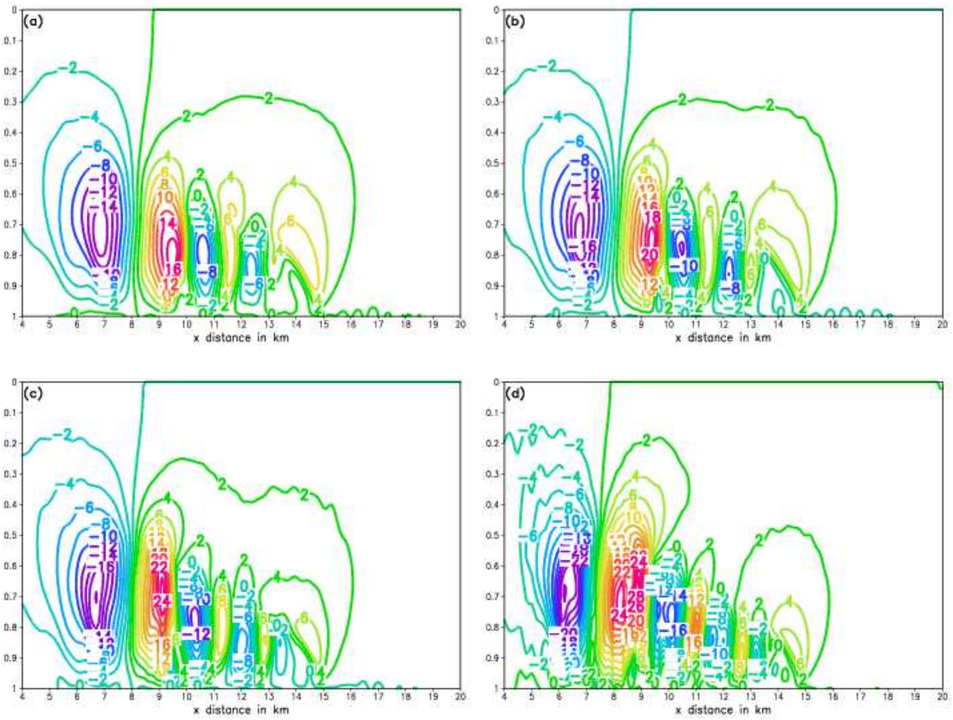

Figure 5.5: The $\hat{w}$ component of the wind for the cold bubble test after 900 s, in the right-hand part of the integration domain, for $0 \leq \sigma \leq 1$: (a) $K_s = 75\,ms^{-2}$; (b) $K_s = 50\,ms^{-2}$; (c) $K_s = 25\,ms^{-2}$; (d) $K_s = 0\,ms^{-2}$. The contour interval is 2 ms^{-1}.

for the case of zero diffusion is somewhat of a concern, since it may indicate the development of nonlinear instability in the simulations. Indeed, simulations with fourth order spatial differencing becomes unstable for $K_s = 0\,m^2s^{-1}$, unless a spatial filter is applied to some of the variables.

5.2.5 The effect of the Shapiro spatial filter

It has long been known that the A-grid used in the present study has poor gravity wave dispersion properties (see Chapter 4). An analysis of the linearized quasi-elastic equations in Chapter 4 has indicated that horizontal centered differencing on the nonstaggered grid results in the frequency (and phase speed) of short wave length gravity waves being significantly retarded, and the two-grid-interval waves are stationary. Higher order differencing leads to significant improvements in representing the true gravity wave properties at wave lengths as short as four grid-intervals, but the two-grid-interval waves remain stationary and problematic. For the linearized quasi-elastic equations, the effect of vertical centered differencing on gravity wave dispersion on the nonstaggered grid is similar to that of horizontal differencing. The vertical two-grid-interval waves are not stationary, however, only significantly retarded. In Chapter 4 the use of a high order Shapiro filter was suggested, to completely remove the two-grid-interval waves from the grid. This filter, when applied at high order, has a negligible effect on the amplitude of the longer wave length waves (see Chapter 4). In this section, the effect of Shapiro filter on the cold bubble simulations is investigated.

The settings of the experiments presented in this section correspond to those of the reference simulation. The only differences are the various values of the diffusion coefficients that are applied, and the fact that the spatial filtering is used. The Shapiro (1975) filter is applied only during the N^{th} time step of each adjustment phase of N time steps. The filter is first applied in the x direction for a specific field, whereafter the horizontally filtered field is filtered along the σ axis by a second application of the filter. The filter is applied to the fields u, $\ln p_s$, $\dot{\sigma}$ and ϕ only (see Chapter 4). The filter with p = 4 is applied, at grid points with stencils that allow this degree of filtering. Near the vertical boundaries, where grid points allow an order of filtering of 3 or less, lower order vertical filtering is performed. Similarly, horizontal filtering with p = 3 or less is performed near the lateral boundaries.

Fig. 5.6 shows the potential temperature perturbation $\theta^{'}$ after t = 900 s, obtained with the settings of the Shapiro filter as described in the previous paragraph. The settings chosen for explicit diffusion used in the tests described here, are the same as for the explicit diffusion tests described in the previous section. That is, diffusion coefficients of $K_s = 75\,m^2s^{-1}$, $K_s = 50\,m^2s^{-1}$, $K_s = 25\,m^2s^{-1}$ and $K_s = 0\,m^2s^{-1}$ were used to obtain the simulations in Panels a to d of Fig. 5.6 respectively. Fig. 5.7 shows the corresponding $\hat{w}$ fields

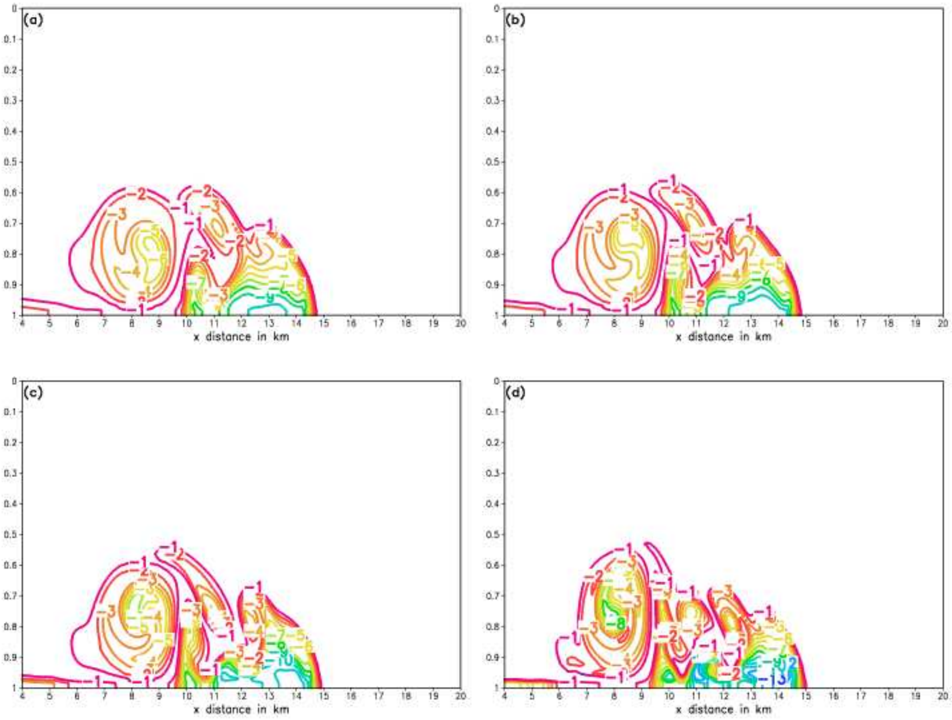

Figure 5.6: The potential temperature deviation after 900 s for the cold bubble test, in the right-hand part of the integration domain, for $0 \leq \sigma \leq 1$: (a) $K_s = 75\,ms^{-2}$; (b) $K_s = 50\,ms^{-2}$; (c) $K_s = 25\,ms^{-2}$; (d) $K_s = 0\,ms^{-2}$. The Shapiro filter is applied with $p = 4$. The contour interval is 1K.

obtained. The extreme values obtained for $\theta^{'}$, u and $\hat{w}$ at t = 900 s are listed in Table 5.2.

The most striking effect of the Shapiro filter, is that simulated $\hat{w}$ fields are much smoother than the corresponding simulations obtained without the use of the filter (compare Fig. 5.7 to Fig. 5.5) . This suggests that the filter has succeeded in removing, at least to a large extent, the effects of stationary two-grid-interval waves on the simulations. However, there is still slight noise present in the $\hat{w}$ fields obtained for the case of zero diffusion (Panel d of Fig. 5.7). It is possible that retarded gravity waves, with wave-lengths near the shortest resolvable scales, contribute to the numerical noise still present in this simulation (e.g. Purser, 1987). However, application of the filter seems to keep the noise to acceptable levels. This is confirmed by the extreme values listed for $\hat{w}$ for the case of zero diffusion (simulation SD in Table 5.2). These extreme values are significantly smaller in magnitude than the values of $\hat{w}$ obtained for the case of zero diffusion without the application of the Shapiro filter (simulation FD in Table 5.1).

By comparing the potential temperature perturbation fields in Figs. 5.4 and 5.6, it may be seen that for a particular choice of diffusion coefficient, application of the Shapiro filter causes some retardation to occur in the time-evolution of the flow field. The same number of rotors are simulated by t = 900 s for all the corresponding cases. However, the time-evolution of the third rotor is slightly slower in the simulations where the Shapiro filtered is applied, compared to the corresponding simulations obtained without application of the filter. The relative positions of the first and second third rotors are different in the simulations obtained with application of the Shapiro filter compared to the simulations obtained without the use of the filter. The trailing edge of the gust front progresses further in the simulations where the Shapiro filter is applied compared to the nonfiltered simulations. However, the leading edge of the gust front has progressed slightly less in the simulations obtained with relatively large diffusion coefficients where the filter is applied (Panels a and b of Fig. 5.6), compared to the corresponding simulations obtained without application of the filter (Panels a and b of Fig. 5.4). For relatively large values of explicit diffusion, the extreme values obtained for $\theta^{'}$, u and $\hat{w}$ with application of the filter, are similar to the values obtained without application of the filter (Compare FA and FB in Table 5.1 to SA and SB in Table 5.2).

From these and other experiments with the Shapiro filter, the following additional conclusions may be drawn:

- applying the spatial filter during each adjustment time-step, slows down the time-evolution of the flow field. For example, for the case $K_s = 50\, m^2 s^{-1}$ the gust front progresses to about 14.3 km in 900 s, instead of about 14.8 km as in the present case (Panel b of Fig. 5.6). Here the filter

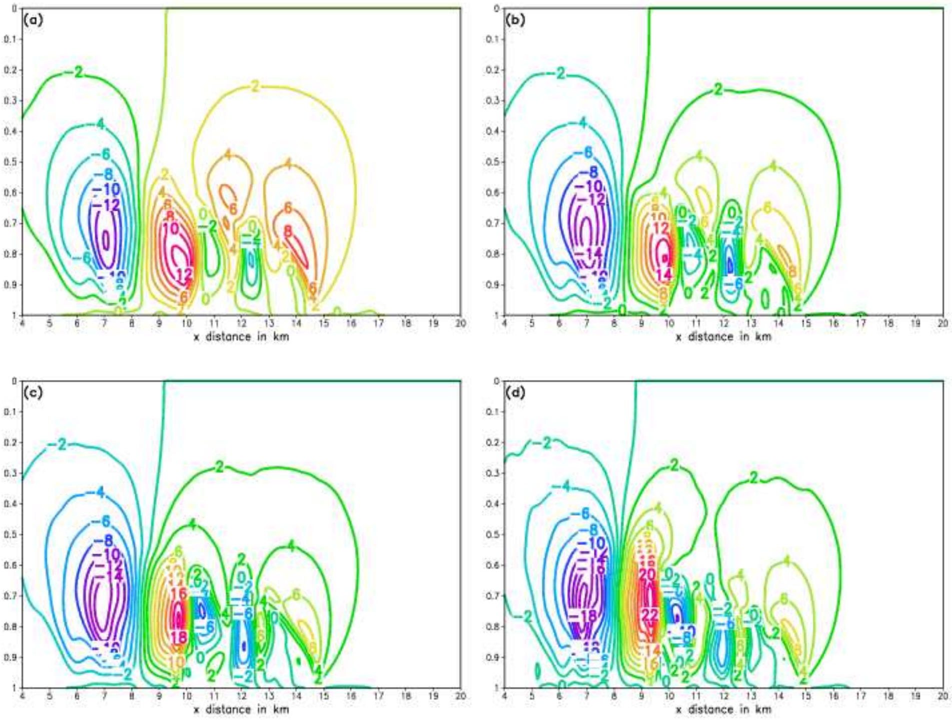

Figure 5.7: The $\hat{w}$ component of the wind for the cold bubble test after 900 s, in the right-hand part of the integration domain, for $0 \leq \sigma \leq 1$: (a) $K_s = 75\, ms^{-2}$; (b) $K_s = 50\, ms^{-2}$; (c) $K_s = 25\, ms^{-2}$; (d) $K_s = 0\, ms^{-2}$. The Shapiro filter is applied with p = 4. The contour interval is 2 ms^{-1}.

is applied only during the N^{th} adjustment time-step. The development of the third rotor is also somewhat retarded if the filter is applied during each adjustment time-step. The progress of the leading edge of the gust front in the present set of experiments is in close agreement to the experiments performed in the previous section where the Shapiro filter was not applied at all (compare Figs. 5.6 and 5.4), especially at relatively low values of explicit diffusion. The time evolution of the two rotors in the two sets of experiments is also similar, except for the case of zero diffusion. Clearly, a balance is needed between applying the filter too often (which somewhat slows down the time evolution of the flow) and applying the filter too infrequently (which leads to the development of two-grid-interval noise - see section 5.2.4). This aspect is investigated further in section 5.2.8;

- applying the Shapiro filter of order $p = 4$, during the N^{th} adjustment time-step only, produces satisfactory results. The noise originating from the two-grid-interval waves is sufficiently controlled, whilst no significant damping effects are visible at longer wave lengths. There seems to be no advantage in spending extra calculations, by filtering at values of p larger than 4, at grid points with stencils that do allow this order of filtering;

- filtering near the vertical boundaries is somewhat problematic. In the present set of experiments, it was found necessary to perform horizontal filtering with $p = 2$ at the row of grid points directly above the lower boundary, at grid points with stencils that do allow a higher order of filtering. Two-grid-interval noise originates near the lower boundary if higher order filtering (or no filtering) is performed along this row of grid points. Similarly, horizontal filtering with $p = 2$ is performed along the row of grid points adjacent to the upper boundary. However, filtering at higher values of p along this row was not found to have a significant impact on the simulations. Vertical filtering with $p = 0, 1, 2$ or 3 is performed near the lower and vertical boundaries, depending on on the order of filtering allowed by the stencils of grid points. It was found that this relatively low order of filtering has only a slight damping effect on the important flow features that are present near the lower boundary.

- filtering near the lateral boundaries, in the region where the stencils around the grid points allow filtering of degree $p = 3$ or less, was found to have a negligible effect on the simulations. This is probably due to the fact that by $t = 900$ s (the end of the integration time), the important flow features are still relatively far away from the lateral boundaries. However, if important flow features are present near the lateral boundaries, filtering in this region by applying the Shapiro filter at relatively low values of p may be problematic. For example, in the case where dynamic (time-dependent) lateral boundary conditions are used, the damping induced by low order filtering may have negative effects on the simulation.

Table 5.2: Comparison of minimum and maximum values of $\theta^{'}$, u and $\hat{w}$ obtained for the various values of explicit diffusion. The values of the diffusion coefficients used are $K_s = 75\, m^2 s^{-1}$ (FA), $K_s = 50\, m^2 s^{-1}$ (FB), $K_s = 25\, m^2 s^{-1}$ (FC) and $K_s = 0\, m^2 s^{-1}$ (FD). The Shapiro filter is applied, with p = 4.

$Variable$	SA	SB	SC	SD
$\theta^{'}_{min}$	-10.32	-10.92	-11.80	-13.56
$\theta^{'}_{max}$	0.07	0.09	0.13	1.45
u_{min}	-14.58	-15.46	-16.80	-19.44
u_{max}	34.81	35.87	36.47	35.68
w_{min}	-14.19	-14.79	-15.95	-18.64
w_{max}	12.68	16.12	20.59	23.39

5.2.6 Advantages to be gained from fourth order spatial differencing

In the experiments presented in the previous sections, all spatial derivatives present in the adjustment step equations were discretized using second order differencing. Stationary two-grid-interval waves, and a significant retardation of the frequency (and phase speed) of gravity waves near the shortest resolvable scales, may therefore be expected to be present in the discretized equations (see Chapter 4). In the previous two sections, it has been shown that the problems arising from these poor gravity wave dispersion properties of the A-grid, such as two-grid-interval noise, may to a large extent be controlled by the use of explicit diffusion and the highly scale-dependent Shapiro filter. The linear analysis presented in Chapter 4 indicates that additional improvements in the numerical representation of gravity wave frequencies near the shortest resolvable scales may be expected from the use of higher order (fourth and sixth order) spatial differencing on the nonstaggered grid. In this section, a fourth order discretization of the adjustment step equations is presented. The advantages to be gained from this higher order discretization (compared to the second order discretization used in the previous sections) are illustrated by means of a series of numerical tests.

In order to obtain a full fourth order discretization of the spatial derivatives in the the adjustment step equations, not only the first derivatives present in these equations, but also the second derivatives that appear in the elliptic equation (3.86) are discretized using fourth order differencing (see Chapter 4 for the appropriate fourth order differencing formulas). Second order vertical differencing needs to be applied at the grid points adjacent to the lower and upper boundaries, since the stencils of these grid points do not allow a higher degree of differencing (unless artifical computational boundaries are introduced). Similarly, second order horizontal differencing needs to be applied at grid points adjacent to the lateral boundaries. Note that for most grid points adjacent to the lateral boundaries, fourth order differencing is used for the vertical derivatives, whilst second order difeerencing needs to be used to discetize the horizontal derivatives. The converse is true for grid points adjacent to the vertical boundaries. It has been found crucial to consistently apply the same order of differencing at each grid point in the domain, for each of the adjustment step equations, for horizontal and vertical differencing respectively. The coding of the fourth order elliptic solver, with mixed second-fourth order differencing applied at grid points adjacent to the vertical and lateral boundaries, was found to be a rather cumbersome exercise.

Fourth-order differencing also implies that more grid points are used in the discretized operator. For example, fourth order discretization of the second derivatives in the elliptic equation (3.86) involves the use 25 grid points. whilst only 9 grid points are needed in the corresponding second order discretization. It is known that the SOR procedure is associated with progressively slower convergence as the number of grid points in the discretized operator increases (Xue, 1989). The efficiency of the fourth order elliptic solver is compared to that of the second order solver in section 5.2.10.

Figure 5.8 shows the potential perturbation at t = 900 s, obtained with the fourth order differencing scheme, for various magnitudes of explicit diffusion as specified in section 5.2.4. That is, diffusion coefficients of $K_s = 75\, m^2 s^{-1}$, $K_s = 50\, m^2 s^{-1}$, $K_s = 25\, m^2 s^{-1}$ and $K_s = 0\, m^2 s^{-1}$ were used to obtain the simulations in Panels a to d of Fig. 5.8 respectively. The Shapiro filter with $p = 4$ was applied, with filtering of lower order used near the vertical boundaries as described in the previous section. Figure 5.9 shows the corresponding results obtained for the $\hat{w}$ field.

The simulations presented in this section are directly comparable to those of the previous section, where the Shapiro filter with $p = 4$ was also applied, but second order differencing was used to discretize the spatial derivatives in the adjustment step equations. For fourth order differencing, the flow features are further evolved than for second order differencing, for each value of the diffusion coefficient used (compare Panels a to d in Fig. 5.8 to the corresponding panels in Fig. 5.6). This significant result may be explained by the fact that for second order differencing, the phase speed of short wave-length gravity waves is significantly retarded. With fourth order differencing, the representation of the analytic gravity wave phase speed is more accurate (see Chapter 4), which leads to the faster evolution of flow features displayed in Fig. 5.8. In the fourth order simulation with zero diffusion, the fourth rotor is better developed than in any of the previously performed simulations, as can be seen clearly from the potential temperature perturbation field in Panel d of Fig. 5.8. The trailing edge of the gust front has broken off from the main pool of cold air travelling

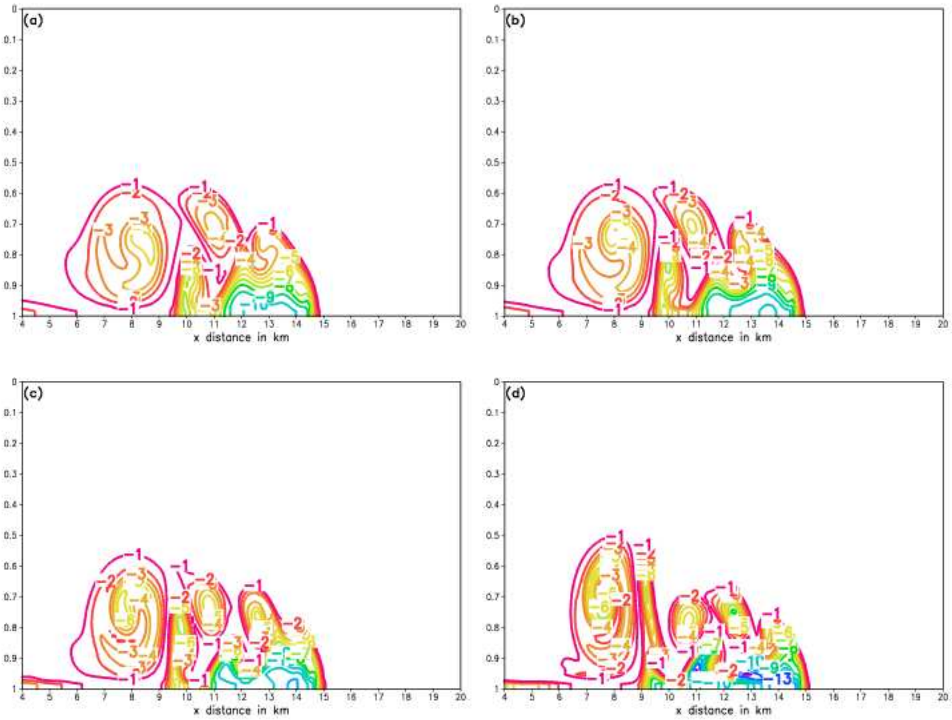

Figure 5.8: The potential temperature deviation after 900 s for the cold bubble test, in the right-hand part of the integration domain, for $0 \leq \sigma \leq 1$: (a) $K_s = 75\,ms^{-2}$; (b) $K_s = 50\,ms^{-2}$; (c) $K_s = 25\,ms^{-2}$; (d) $K_s = 0\,ms^{-2}$. The fourth order discretization of spatial derivatives in the adjustment step equations and the Shapiro filter with $p = 4$ were used. The contour interval is 1K.

Table 5.3: Comparison of minimum and maximum values of $\theta^{'}$, u and $\hat{w}$ obtained when fourth order discretization of spatial derivatives is applied. The Shapiro filter with $p = 4$ is used. The values of the diffusion coefficients used are $K_s = 75\,m^2s^{-1}$ (FA), $K_s = 50\,m^2s^{-1}$ (FB), $K_s = 25\,m^2s^{-1}$ (FC) and $K_s = 0\,m^2s^{-1}$ (FD).

$Variable$	FA	FB	FC	FD
$\theta^{'}_{min}$	-10.55	-11.19	-12.18	-14.15
$\theta^{'}_{max}$	0.07	0.10	0.19	1.50
u_{min}	-14.79	-15.81	-17.77	-19.64
u_{max}	34.29	35.24	35.00	32.04
w_{min}	-14.87	-15.52	-16.64	-18.36
w_{max}	13.69	17.44	21.15	26.89

in the horizontal near the surface, and has been flung into the vertical by the first rotor's updraft. This feature is also present in the corresponding simulation obtained with second order differencing, however.

As in the case of second order differencing with application of the Shapiro filter, the $\hat{w}$ fields in Fig. 5.9, are much less noisy than the fields obtained with second order differencing without the use of the Shapiro filter (compare in particular Panels c to d of Fig. 5.9 to the corresponding panels of Fig. 5.5). There is also no excessive growth in the amplitudes of the $\theta^{'}$, u, and $\hat{w}$ fields obtained for the case zero diffusion (see Table 5.3). Thus, it seems as if the Shapiro filter controls the noise originating from the nonstaggered grid, also for the case of the fourth order spatial differencing. A comparison of the extreme values listed in Table 5.3 (fourth order differencing) to those in Table 5.2 (second order differencing) shows very close agreement, even for the case of zero diffusion. The slightly larger differences in the zero diffusion case may be attributed to the further evolved flow field obtained for the case of fourth order differencing at t = 900 s, compared to the field obtained with second order differencing.

It may be said that the Shapiro filter with p = 4 effectively removes two-grid-interval waves on the nonstaggered grid, for both the cases of second and fourth order spatial differencing. In the case of second order differencing with application of the Shapiro filter, the time-evolution of the flow features is somewhat retarded compared to the corresponding nonfiltered solutions. In this regard, the fourth order simulations with application of the Shapiro filter offers an improvement over second order differencing. In the former case, the improved representation of the gravity wave phase speed leads to more accurate and further evolved flow fields at t = 900 s, for each particular design of explicit diffusion used.

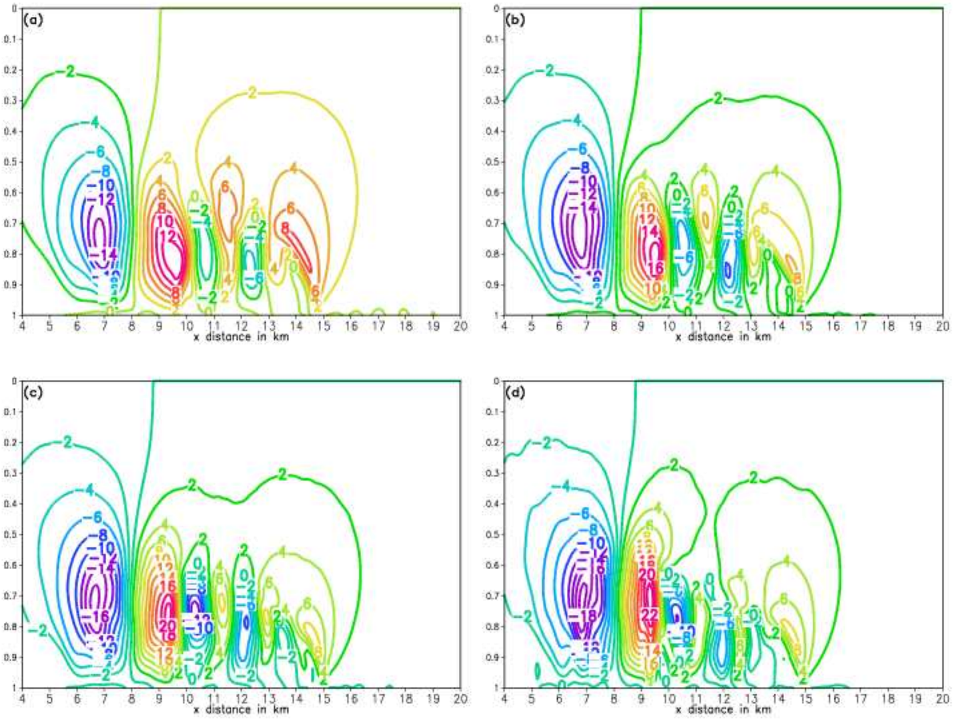

Figure 5.9: The $\hat{w}$ component of the wind for the cold bubble test after 900 s, in the right-hand part of the integration domain, for $0 \leq \sigma \leq 1$: (a) $K_s = 75\,ms^{-2}$; (b) $K_s = 50\,ms^{-2}$; (c) $K_s = 25\,ms^{-2}$; (d) $K_s = 0\,ms^{-2}$. The fourth order discretization of spatial derivatives in the adjustment step equations and the Shapiro filter with $p = 4$ were used. The contour interval is 2 ms^{-1}.

5.2.7 The effect of the choice of D_N scheme

The most simple way of calculating the departure points at time level τ in a semi-Lagrangian discretization of the two-dimensional atmospheric equations, is by using the formula

$$\begin{bmatrix} x^* \\ \sigma^* \end{bmatrix} = \begin{bmatrix} x \\ \sigma \end{bmatrix} - \Delta t \begin{bmatrix} u^\tau \\ \dot{\sigma^\tau} \end{bmatrix}. \tag{5.5}$$

Here $\left(u^\tau,\, \dot{\sigma^\tau}\right)$is the time level τ wind field, which is assumed to remain constant over the time interval $(\tau,\, \tau + \Delta t)$. This way of calculating the departure points will be referred to as the D_0 scheme. It is interesting to investigate the advantages that can be gained over the D_0 scheme in the cold bubble simulations, by using the D_N schemes of McGregor (1993). In the D_N schemes the approximated velocity at time level $\tau + \Delta t/2$ (and its approximated total time derivatives of various order for the higher order D_N schemes) are used to calculate the departure points (see Chapter 4). In all the experiments described in the previous sections, the D_3 scheme was used. The spatial derivatives that occur in the two-dimensional form of the calculation formula (4.8) for the D_3 scheme and the term $A^*_{p_s}$ (see Chapter 4), were evaluated using second order differencing. In combination with the question of most suitable choice of D_N scheme, the question arises whether more accurate results can be expected by using fourth order spatial differencing in the calculation of the term $A^*_{p_s}$ and the departure point formulas (4.7) and (4.8) of the D_2 and D_3 schemes.

The resolution and general design of the experiments performed in this section are as described for the reference solution (see section 5.2.3). The settings of explicit diffusion along the x and σ axis are as described in section 5.2.4, with $K_s = 25\, m^2 s^{-1}$. The Shapiro filter is used, with the settings as described in section 5.2.5. Fourth order spatial differencing is used in the adjustment step, as described in section 5.2.6. Fig. 5.10 shows the potential temperature perturbation at t = 900 s obtained using respectively the D_0 scheme (Panel a), D_1 scheme (Panel b) and D_2 scheme (Panel c). Here second order differencing was applied to the spatial derivatives in the departure point formulas and the term $A^*_{p_s}$. The D_3 scheme with fourth order spatial differencing applied to the departure point formulas and the term $A^*_{p_s}$ was used to obtain the simulation depicted in Panel d of Fig. 5.10. The corresponding $\hat{w}$ fields are displayed in Fig. 5.11. These results may be compared to the corresponding solution obtained using the D_3 scheme with second order spatial differencing applied to the departure point formula and the term $A^*_{p_s}$ (Panels c of Figs. 5.8 and 5.9). The extreme values obtained for $\theta^{'}$, u and $\hat{w}$ are listed in Table 5.4 for the D_0, D_1 and D_2 schemes. The D_3 scheme with fourth order spatial differencing applied to the departure point formula and the term $A^*_{p_s}$is denoted by D_{3F} in the Table 5.4. Note that corresponding results obtained with the D_3 scheme, but with second order differencing applied to the departure point formula and the term A_{p_s}, are displayed in column FC of Table 5.3.

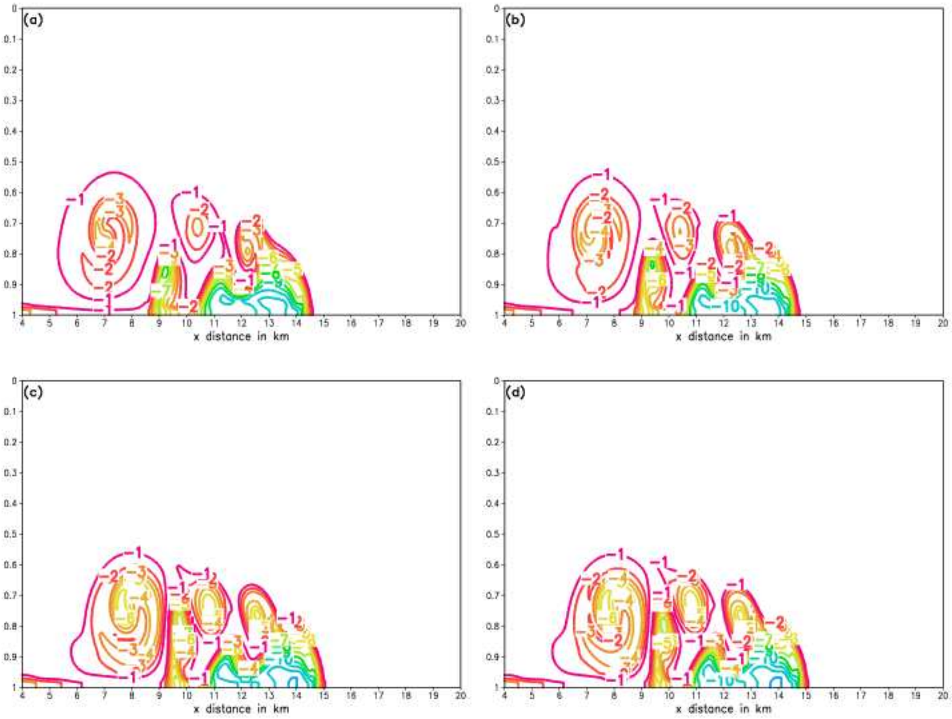

Figure 5.10: The potential temperature deviation after 900 s for the cold bubble test, in the right-hand part of the integration domain, for $0 \leq \sigma \leq 1$: (a) D_0 scheme; (b) D_1 scheme; (c) D_2 scheme; (d) D_3 scheme with fourth order differencing applied to the departure point formula and the term $A^*_{p_s}$. The fourth order discretization of spatial derivatives in the adjustment step equations and the Shapiro filter with $p = 4$ are used. $K_s = 25\, m^2 s^{-1}$. The contour interval is 1K.

There are mainly three conclusions that can be drawn from the experiments presented in this section:

- the results obtained from using respectively the D_2 and D_3 schemes to calculate the departure points are almost indistinguishable (Compare Panels c of Figs. 5.10 and 5.11 to Panels c of Figs. 5.8 and 5.9). Even the relevant extreme values listed in Tables 5.4 and 5.3 (columns D_2 and FC respectively) show very close correspondence. Thus, at least in the present of set experiments, there seems to be no advantage in going beyond the D_2 scheme to calculate the departure points in the split semi-Lagrangian procedure.

- The differences are negligible between the results obtained when the D_3 scheme is used with second order differencing applied to the spatial derivatives in the departure point formula and term $A^*_{p_s}$, compared to when the D_3 scheme is used with fourth order differencing applied to the relevant derivatives (compare Panels c of Figs. 5.8 and 5.9 to Panels d of Figs. 5.10 and 5.11). Even the relevant extreme values listed in Tables 5.3 and 5.4 (columns FC and $\mathrm{D}_{3\mathrm{F}}$ respectively) show very close correspondence. Clearly, there seems to be no advantage in going beyond second order spatial differencing when calculating the spatial derivatives in the departure point formula and term $A^*_{p_s}$.

- the D_0 and D_1 schemes (Panels a and b of Figs. 5.10 and 5.11) produce reasonable results, but there are some important differences with the corresponding D_2 and D_3 simulations (Panels c of Figs. 5.10 and 5.11 and Panels c of Figs 5.8 and 5.9). For example, the gust front in the D_0 and D_1 simulations progresses slightly slower than in the corresponding D_2 and D_3 simulations, and the maximum amplitude of the updraft of the first rotor is weaker in the D_0 and D_1 simulations than in the D_2 and D_3 simulations. Most important perhaps, is the much steeper gradient in the potential temperature perturbation field present in the D_2 and D_3 simulations, compared to the corresponding D_0 and D_1 fields. It may be said that the D_0 and D_1 schemes produce excessive smoothing of the potential temperature perturbation field, compared to the D_2 and D_3 schemes. Thus, stronger amplitude damping and phase retardation (with respect to the advection process) seems to be caused by the D_0 and D_1 schemes, compared to the D_2 and D_3 schemes.

It may be noted that in the experiments of McGregor (1993) it was found sufficient to use the D_3 scheme with second order spatial differencing applied to the spatial derivatives in the departure point formula. In these experiments, and in the regional climate model DARLAM and variable resolution global model C-CAM, the D_3 scheme is used only for the simulation of horizontal advection (see McGregor, 1993, 1996; McGregor and Dix, 2001). Huang (1994) applied the D_2 scheme for horizontal advection in a series of numerical tests that investigated the use of various interpolation methods in semi-Lagrangian advection schemes.

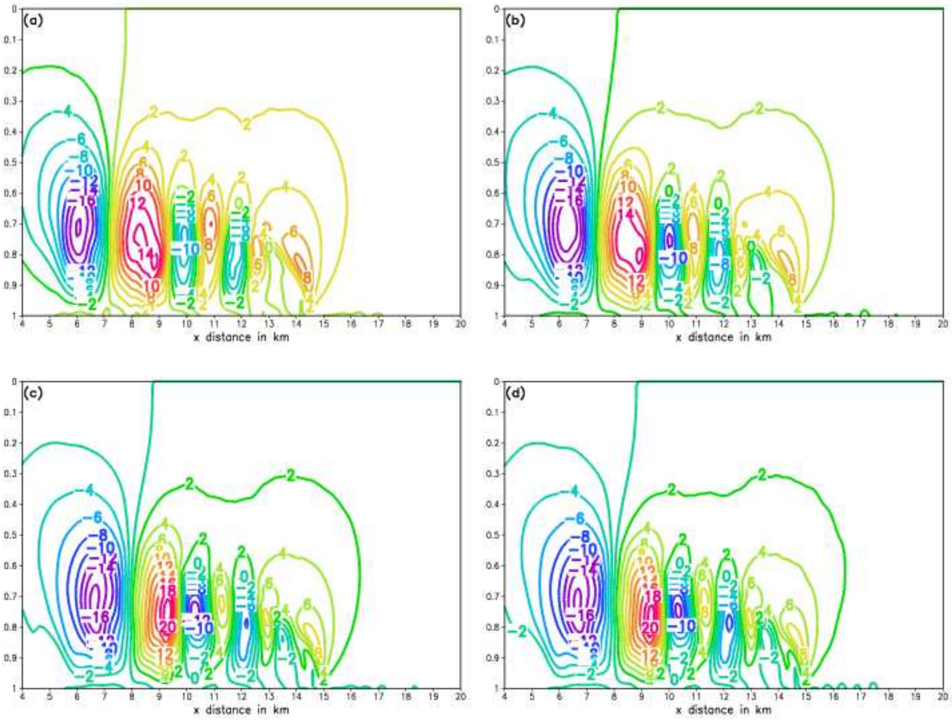

Figure 5.11: The $\hat{w}$ component of the wind after 900 s for the cold bubble test, in the right-hand part of the integration domain, for $0 \leq \sigma \leq 1$: (a) D_0 scheme; (b) D_1 scheme; (c) D_2 scheme (d) D_3 scheme with fourth order differencing applied to the departure point formula and the term $A^*_{p_s}$. The fourth order discretization of spatial derivatives in the adjustment step equations and the Shapiro filter with $p = 4$ are used. $K_s = 25\, m^2 s^{-1}$. The contour interval is 2 ms^{-1}.

Table 5.4: Comparison of minimum and maximum values of θ', u and $\hat{w}$ obtained for the various departure point schemes. The fourth order discretization of spatial derivatives in the adjustment step equations and the Shapiro filter with $p = 4$ are used. $K_s = 25\,m^2 s^{-1}$.

$Variable$	D_0	D_1	D_2	D_{3F}
θ'_{min}	-11.50	-11.79	-12.14	-12.21
θ'_{max}	0.35	0.19	0.17	0.17
u_{min}	-17.41	-17.78	-17.85	-17.56
u_{max}	32.26	33.31	34.79	35.69
w_{min}	-18.19	-17.95	-16.66	-16.42
w_{max}	14.49	16.53	21.70	21.10

5.2.8 Marginally and poorly resolved flow

Operational weather prediction beyond the hydrostatic limit (horizontal resolutions finer than about 15 km) has become a reality at meteorological institutions all over the world. However, even at the largest meteorological centers, it would not in the foreseeable future be possible to integrate global nonhydrostatic models at resolutions where convection can be fully resolved (horizontal and vertical resolutions of a few hundred meters or finer). Even for the case of regional-scale NWP and climate simulation, horizontal resolution of a few kilometers at best is likely to be the only practical choice for many years to come (see the discussion in Chapter 1). Thus, nonhydrostatic regional models will most probably be integrated at resolutions where convection can only be poorly, or at best marginally, resolved. Conversely, hydrostatic models have traditionally been used at low spatial resolutions where convection is not resolved at all. Most of the parameterization schemes used in these models to represent the effects of convection on the atmosphere have therefore been developed to function well at relatively low spatial resolutions, where convection is not explicitly resolved. However, with the advent of nonhydrostatic models and the increase in model resolution, convection schemes are now required to function well in a model atmosphere where convection is marginally resolved. This is likely to become an increasingly important new focus area in numerical weather simulation in the near future (see Chapter 1). Even more fundamental, is the ability of the numerical solution procedure used in the model to perform well in the case of marginally or poorly resolved convection. In the present section, the performance of the split semi-Lagrangian scheme in the cold bubble downburst problem is investigated, for the cases of marginally and poorly resolved flow.

In all the experiments performed in this section, the D_3 scheme of McGregor (1993) with bicubic spatial interpolation is applied in the advection step. Second order differencing is used to discretize the spatial derivatives in the departure point formula and the term $A^*_{p_s}$. The Shapiro filter with p = 4 is used, with lower order filtering performed near the boundaries as described in section 5.2.5. The explicit diffusion applied along both the x and σ axis is as described in section 5.2.4, with $K_s = 50\,m^2s^{-1}$.

In order to simulate the basic flow structures of the diffusion limited cold bubble downburst problem, Straka et al. (1993) found that the grid spacing should be at least 133.3 m (in both the horizontal and vertical). At coarser resolutions, the basic flow features (that is, the development of the three rotors) are not fully captured. They found that at 200 m grid spacing the flow is marginally resolved, and poorly resolved at 400 m grid spacing. The first two experiments performed in this section employ a horizontal grid spacing of 200 m; 33 σ levels are used to give an average grid spacing of 200 m in the vertical. The advection time-step is $\Delta t_s = 2\,s$ and the adjustment time-step is $\Delta t_a = 0.2\,s$. Thus, the ratios $\Delta t_s/\Delta x$ and $\Delta t_a/\Delta x$ used in the previous sections are kept constant. The potential temperature perturbation after t = 900 s obtained with these settings, for second and fourth order spatial differencing applied to the adjustment step equations respectively, are shown in Panels a and b of Fig. 5.12. The corresponding $\hat{w}$ fields are shown in Panels a and b of Fig. 5.13 respectively.

In the third experiment performed, the horizontal grid spacing used is 400 m, and 17 σ levels are used to give an average grid spacing of 400 m in the vertical. Here the advection time-step is $\Delta t_s = 4\,s$ and the adjustment time-step is $\Delta t_a = 0.4\,s$. The potential temperature perturbation after t = 900 s for the 400 m simulation is shown in Panel c of Fig. 5.12. Fourth order spatial differencing is applied to the adjustment step equations. The corresponding $\hat{w}$ field is shown in Panel c of Fig. 5.13. In the final experiment performed in this section, the horizontal grid spacing used is 500 m and 65 σ levels are used as in the previous sections, in order to give a vertical grid spacing of about 100 m. Fourth order spatial differencing is applied to the adjustment step equations. This test will be useful for later comparison to three-dimensional cold bubble simulations. The fourth experiment also corresponds to the current situation in operational NWP and climate simulation, where computational constraints generally determine that models are integrated at relatively low horizontal resolutions, compared to the vertical resolution. The solutions obtained in this section may be compared to the corresponding 100 m solutions that were obtained using second order differencing (Panel b of Fig. 5.8) and fourth order differencing (Panel b of Fig. 5.8).

Two rotors have developed by t = 900 s in the 200 m solution obtained with second order differencing applied to the adjustment step equations (Panel a of Fig. 5.13). In the corresponding 200 m solution obtained with fourth order differencing applied to the adjustment step equations, a third rotor has almost fully developed by t = 900 s (Panel b of Fig. 5.13). The presence of two well de-

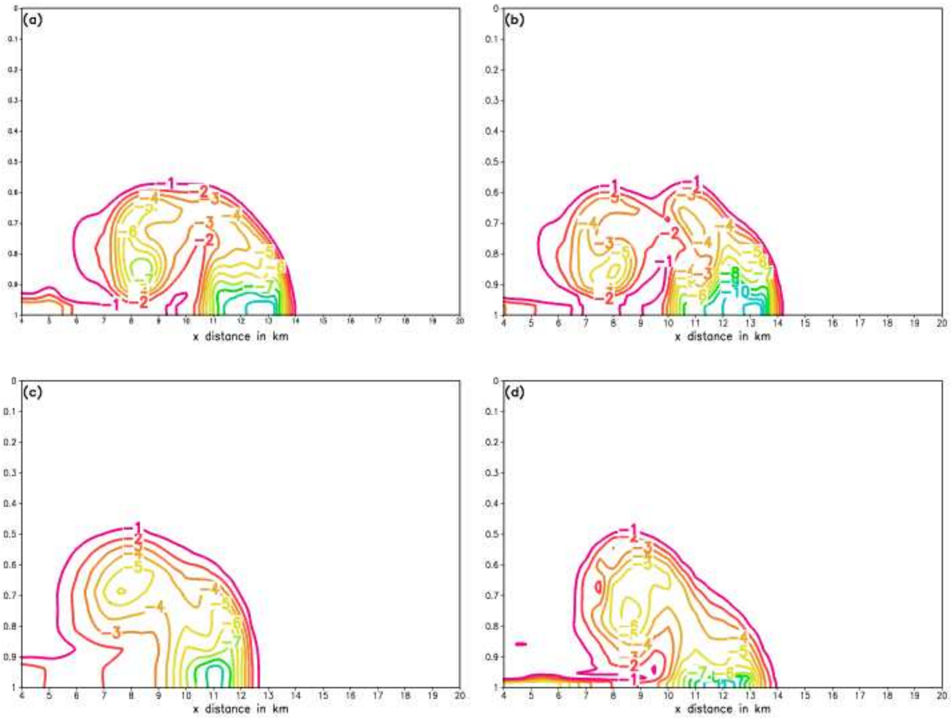

Figure 5.12: Marginally and poorly resolved flow in the cold bubble test. The potential temperature deviation after 900 s in the right-hand part of the integration domain, for $0 \leq \sigma \leq 1$: (a) $\Delta z \approx \Delta x = 200\,m$ with second order differencing; (b) $\Delta z \approx \Delta x = 200\,m$ with fourth order differencing; (c) $\Delta z \approx \Delta x = 400\,m$ with fourth order differencing; (d) $\Delta z \approx 100\,m$, $\Delta x = 500\,m$ with fourth order differencing. The D_3 scheme with second order discretization of spatial derivatives was used in the advection step. The Shapiro filter with $p = 4$ was used. $K_s = 50\,m^2 s^{-1}$. The contour interval is 1 K.

veloped rotors in the case of fourth order differencing can be seen in the relevant potential temperature perturbation (Panel b of Fig. 5.4). In the corresponding second order solution (Panel a of Fig. 5.12), the second rotor is only starting to impact on the potential temperature field. The further evolved flow field in the case of fourth order differencing shows that fourth order differencing offers a significant advantage over second order differencing in these relatively low resolution simulations.

By comparing the flow features displayed in Panel b of Fig. 5.12 to Panel b of Fig. 5.8 (obtained at 100 m resolution), it may be said that in the 200 m simulation the flow features are marginally resolved. The flow pattern is coherent and quite similar to the 100 m solution. However, only two fully developed rotors are simulated in the 200 m solution, in comparison to the three fully developed rotors present in the 100 m solution. The gust front has progressed more slowly in the 200 m solution, to a distance of about 14 km from the center of the x axis, in stead of 15 km as in the 100 m solution. The 200 m solution is dissipative compared to the 100 m solution, as is evident from comparing the 200 m resolution extreme values of $\theta^{'}$, u and $\hat{w}$ listed in Table 5.5 (column M-4) to the corresponding 100 m resolution extreme values (column FB in Table 5.3). The 400 m solution is even more dissipative (see Panel c of Fig. 5.12 and column P of Table 5.5). The gust front progresses even more slowly in the 400 m resolution solution, to a distance of 13 km away from the center x axis. The presence of one rotor in the 400 m resolution solution at t = 900 s can be deduced from the relevant potential temperature perturbation field (Panel c of Fig. 5.12). The corresponding $\hat{w}$ field shows that a second rotor is developing , with only a weak downdraft present at t = 900 s. The solution obtained with 500 m horizontal and on average 100 m vertical resolution (Panels d of Figs. 5.12 and 5.13) is similar to the 400 m solution. Only one fully developed rotor is present at t = 900 s, with a second rotor starting to impact on the leading edge of the gust front. The propagation speed of the gust front corresponds more closely with the 200 m solution than with the 400 m solution, however. The extreme values that correspond to the 500 m horizontal - 100 m vertical simulations (column PM in Table 5.5) correspond more closely to the 200 m solutions than to the 400 m solutions (columns M-4 and P of Table 5.5 respectively).

The main reason for the dissipativeness of the 200 m and 400 m solutions, is the strong damping at high wave numbers that results from the bicubic interpolations used in the semi-Lagrangian advection step (see Chapter 4). At 200 and 400 m grid spacing, the shortest resolvable wave-length waves (that are damped most) carry a more important part of the energy of the system than the shortest resolvable waves in the 100 m grid spacing simulations. The delayed development of flow features in the 200 and 400 m simulations may be attributed to the phase speed damping of the shortest resolvable gravity waves (with the highest wave numbers) on the nonstaggered grid. Once again, the highest wave numbers in the case of the 200 and 400 m simulations represent longer wave length waves that carry more energy than the highest wave number waves in the 100 m simulation. The slower progress of the gust front in the lower resolution simulations compared to the 100 m simulation, is probably the result of the relatively more important phase damping of the high wave number gravity waves and phase damping of the advected fields by the bicubic interpolation scheme. Both the 200 and 400 m solutions at t = 900 s are smooth and without any signs of numerical noise.

A variety of numerical solution procedures have been tested by Straka et al. (1993) for the cases of poorly, marginally and adequately resolved flow. They found that models with damped advection schemes produce smooth flow structures for the case of poorly resolved flow (similar to the results obtained with the split semi-Lagrangian scheme). However, high-order finite difference models produced noisy or unstable results, whilst the results obtained with local spectral and spectral models were essentially unusable. For the case of marginally resolved flow, it was found that the schemes with damped advection schemes produced only two Kelvin-Helmholtz rotors, similar to the results obtained here with the split semi-Lagrangian scheme. They found that high order finite difference and spectral models correctly simulate three rotors at t = 900 s for the case of marginally resolved flow, but the simulations are noisy. The local spectral model performed best, but had problems with energy accumulation at the highest wave numbers. For the case of adequately resolved flow, the high order finite difference, spectral and local spectral methods performed well. For the models with damped advection schemes the flow features were underdeveloped and moved too slow. The split semi-Lagrangian scheme is different in this respect from the models with damped advection schemes studied by Straka et al. (1993), since although also employing a damped advection scheme, three Kelvin-Helmholtz rotors are fully developed at t = 900 s. This corresponds to the 100 m resolution simulations obtained by Straka et al. (1993) using high-order finite difference and spectral models.

It appears as if the split semi-Lagrangian scheme presented here is unique in the sense that it produces acceptable results for all the cases of adequately, margianally and poorly resolved flow. For adequately resolved flow (100 m grid spacing) the flow features are fully developed in comparison to the grid-converged solutions of Straka et al. (1993) and the solutions of Gallus and Rancic (1994) and Janjic et al. (2003). At coarser resolutions, the results are dissipative, but usable, smooth and without any signs of numerical noise.

5.2.9 Time-step experiments and stability tests

In all the experiments performed so far, the maximum values attained by the horizontal and vertical advection Courant numbers (see Chapter 4) during the 900 s integration period are about 0.45 and 0.25 respectively (see section 5.2.3). It may be noted that the advection time-step $\Delta t_s = 1\,s$ employed in these

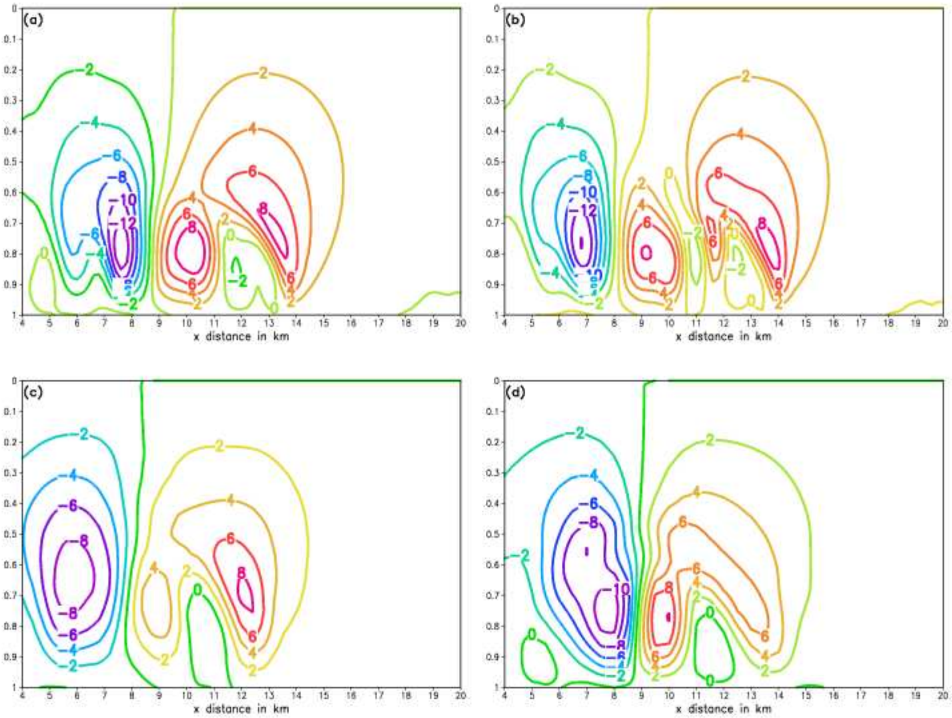

Figure 5.13: Marginally and poorly resolved flow in the cold bubble test. The $\hat{w}$ component of the wind after 900 s in the right-hand part of the integration domain, for $0 \leq \sigma \leq 1$: (a) $\Delta z \approx \Delta x = 200\,m$ with second order differencing; (b) $\Delta z \approx \Delta x = 200\,m$ with fourth order differencing; (c) $\Delta z \approx \Delta x = 400\,m$ with fourth order differencing; (d) $\Delta z \approx 100\,m$, $\Delta x = 500\,m$ with fourth order differencing. The D_3 scheme with second order discretization of spatial derivatives was used in the advection step. The Shapiro filter with $p = 4$ was used. $K_s = 50\,m^2s^{-1}$. The contour interval is 2 ms^{-1}.

Table 5.5: Comparison of minimum and maximum values of $\theta^{'}$, u and $\hat{w}$ for the cases of marginally and poorly resolved flow. The spatial resolutions corresponding to the listed values are $\Delta z \approx \Delta x = 200\,m$ (M-2 and M-4), $\Delta z \approx \Delta x = 400\,m$ (P) and $\Delta z \approx 100\,m$, $\Delta x = 500\,m$ (PM). Fourth order differencing was used to discretize the adjustment step equations, except for simulation M-2, where second order differencing was used.

$Variable$	M-2	M-4	P	PM
$\theta^{'}_{min}$	-10.94	-11.60	-9.35	-11.21
$\theta^{'}_{max}$	0.32	0.34	0.65	1.03
u_{min}	-14.37	-13.80	-12.48	-14.82
u_{max}	34.38	33.91	21.18	29.18
w_{min}	-13.56	14.03	-8.84	-11.28
w_{max}	9.70	9.07	8.56	10.05

experiments is considerably larger than the size of the advection time-steps used in the cold bubble solutions shown by Gallus and Rancic (1996) and Janjic et al. (2001). In both these studies, split-explicit techniques are used to solve the fully-elastic equations cast in vertical coordinates based on the hydrostatic pressure field, with Eulerian procedures employed for the advection terms. Janjic et al. (2001) used a time-step of 0.3 s, whilst Gallus and Rancic (1996) used "an advection time-step twice the sound wave time-step". Gallus and Rancic state that they obtained similar results using an advection time-step as large as 16 times the sound wave time-step, provided diffusion or filtering is increased. They found that this results in small damping of the meteorologically significant features. However, for general atmospheric applications, fully-elastic models employing split-explicit techniques with Eulerian procedures for the advection would be limited to ratios of about 4:1 between the advection and sound wave time steps (Janjic et al., 2001; also see Chapter 4).

In a series of mountain wave experiments using explicit techniques, Room et al. (2001) found the σ coordinate MP model stable at advection Courant numbers varying between 0.005 and 0.024, whilst the NHAD model was stable at advection Courant numbers varying between 0.025 and 0.3. Thus, the values of Courant numbers in the experiments performed so far in the present study, associated with the time-step $\Delta t_s = 1\,s$, are relatively large. It is interesting to investigate the performance of the split semi-Lagrangian scheme at even larger advection time-steps and Courant numbers, in order to quantify the advantages to be gained from the semi-Lagrangian approach used for the advection terms. It is also useful to investigate the performance of the scheme at larger adjustment time-steps. Since the quasi-elastic equations are filtered of vertically propagating acoustic modes, it may be expected that larger adjustment time-steps can

Table 5.6: Stability experiments $\Delta t_s = \Delta t_a$ for various simulations as described in the text.

Differencing and Filtering		TA	TB	TC	TD
SO	Δt_{s_max}	1.6	1.5	1.5	Unstable
	HC	0.69	0.64	0.65	-
	VC	0.54	0.53	0.58	-
SH	Δt_{max}	1.7	1.7	1.7	1.6
	HC	0.75	0.76	0.77	0.91
	VC	0.53	0.58	0.63	0.79
FH	Δt_{max}	1.2	1.2	1.2	1.2
	HC	0.48	0.48	0.50	0.52
	VC	0.36	0.38	0.41	0.45

be used compared to what would be allowed in similar discretizations of the fully-elastic equations. The maximum size of the adjustment time-step used in the split semi-Lagrangian formulation may be expected to be determined by the fast propagating Lamb and gravity waves described by the quasi-elastic equations.

The ratio $\Delta t_s/\Delta t_a$ was 10 in all the previously performed experiments. In addition to the stability tests performed in this section, it is interesting to investigate the performance of the split semi-Lagrangian scheme for different ratios of $\Delta t_s/\Delta_a$.

The resolution and general design of the experiments described in this section are as for the reference solution (see section 5.2.3). In the first set of experiments performed, $\Delta t_s = \Delta t_a$. Working in increments of 0.1 s, a large number of experiments with increasingly larger time-steps was performed, until numerical stability was destroyed within the 900 s integration period. These experiments were performed for the different choices of diffusion coefficients described in section 5.2.4, applied separately to the cases of second order differencing without application of the Shapiro filter (simulations SO), second order differencing with application of the Shapiro filter after each time-step (simulations SH), and fourth order differencing with application of the Shapiro filter after each time-step (simulations FH). The maximum allowable time-steps for the various numerical configurations are displayed in Table 5.6. The associated maximum horizontal and vertical advection Courant numbers attained during the 900 s integration period are also listed in the table. Columns TA, TB, TC and TD in the Table represent respectively diffusion coefficients of $K_s = 75\,m^2s^{-1}$, $K_s = 50\,m^2s^{-1}$, $K_s = 25\,m^2s^{-1}$ and $K_s = 0\,m^2s^{-1}$.

A few conclusions may be drawn from Table 5.6:

- a comparison between the SO and SH results reveals that application of the Shapiro filter results in only a slight increase in the maximum allowable time-step $\Delta t_s = \Delta t_a$, in simulations where explicit diffusion is applied (columns TA to TC). Clearly, the use of explicit diffusion effectively suppresses the nonlinear stability that may develop in association with two-grid interval noise. If no explicit diffusion is used, the SO simulation is unstable, whilst the SH simulation is stable with a maximum allowable time-step similar to the SH and SO cases where explicit diffusion is applied. This points to an efficient removal of two-grid-interval waves by the Shapiro filter in the case of zero explicit diffusion;

- in the stable SO, SH and FH simulations, the maximum advection Courant numbers generally decrease only slightly with an increase in the magnitude of explicit diffusion used (an exception is the SH simulation obtained with zero explicit diffusion and $t_s = t_a = 1.6\,s$, which is on the verge of becoming unstable at t = 900 s). Thus, the explicit diffusion used has only a small damping effect on the extreme values reached by the horizontal and vertical winds. This conclusion is related to the results in sections 5.2.4, 5.2.5 and 5.2.6, where the displacement of the gust front at t = 900 s became only slightly smaller with an increase in the explicit diffusion used. It may be said that the explicit diffusion has only a small damping effect on the wind field and the advection process. However, it was illustrated in sections 5.2.4 to 5.2.6 that the use of explicit diffusion may considerably retard the gravity wave phase speed and the time evolution of the Kelvin-Helmholtz intability rotors;

- the FH scheme becomes unstable at smaller time-steps $\Delta t_s = \Delta t_a$ than the SO and SH schemes. This may be due to the more accurate representation of the gravity wave phase speed when fourth order differencing is used, compared to the more retarded gravity wave phase speed asscociated with the second order discretizations (see Chapter 4).

Figure 5.14 shows the potential temperature perturbation at t = 900 s for some of the time-step experiments performed. The fields in Panels a to c were obtained using second order differencing with time-steps of respectively $\Delta t_s = \Delta t_a = 0.5\,s$, $\Delta t_s = \Delta t_a = 1\,s$ and $\Delta t_s = \Delta t_a = 1.5\,s$. The field in Panel d was obtained using fourth order differencing, with $\Delta t_s = \Delta t_a = 1\,s$. In all the simulations the Shapiro filter with $p = 4$ was applied after each time-step (see section 5.2.5). $K_s = 50\,m^2 s^{-1}$.

A few conclusions may be drawn from considering the results depicted in Figure 5.14, and the corresponding simulations obtained with time steps $\Delta t_s = 1\,s$, $\Delta t_a = 0.1\,s$ (Panel b of Fig. 5.6 for second order differencing and Panel b of Fig. 5.8 for fourth order differencing):

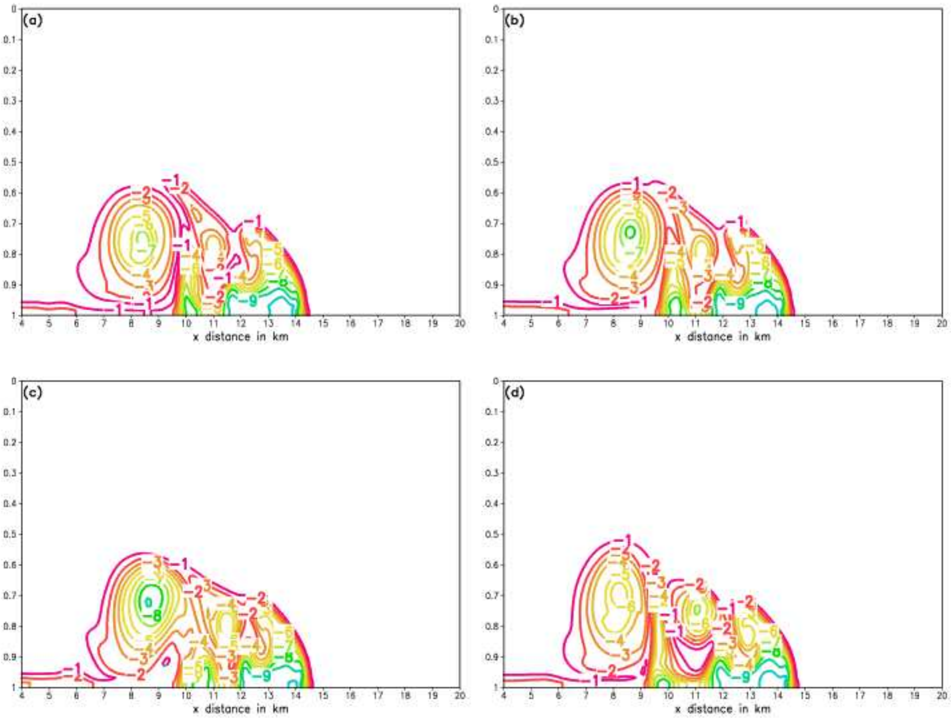

Figure 5.14: The potential temperature deviation after 900 s for the cold bubble test, in the right-hand part of the integration domain, for $0 \leq \sigma \leq 1$: (a) SH simulation with $\Delta t_s = \Delta t_a = 0.5\,s$; (b) SH simulation with $\Delta t_s = \Delta t_a = 1\,s$; (c) SH simulation with $\Delta t_s = \Delta t_a = 1.5\,s$; (d) FH simulation with $\Delta t_s = \Delta t_a = 1\,s$. The Shapiro filter with $p = 4$ was used, with $K_s = 50\,m^2s^{-1}$. The contour interval is 1K.

- the progress of the gust front in all the simulations with $\Delta t_s = \Delta t_a$ is somewhat slower by t = 900 s than in the corresponding simulations with $\Delta t_s = 1\,s$ and $\Delta t_a = 0.1\,s$. Simulations with $\Delta t_s = \Delta t_a$ where the Shapiro filter is applied less frequently, or not at all, show similar behaviour. Thus, the slower progress of the gust front in the $t_a = t_s$ simulations is likely to be the result of the damping at high wave numbers exerted by the bicubic spatial interpolations used in the semi-Lagrangian advection step (see Chapter 4). The effect of the damping nature of the advection scheme appears to be less if an adjustment time-step smaller than the advection time-step is used (see Panels b of Figs. 5.6 and 5.8). In such a case, flow features may develop more unhindered (by damping) during the adjustment process.

- Three rotors are simulated at t = 900 s in all the experiments performed with $\Delta t_s = \Delta t_a = 1\,s$ (Fig. 5.14), in correspondence to the simulations obtained with $\Delta t_s = 1\,s$, $\Delta t_a = 0.1\,s$ (Panels b of Figs. 5.6 and 5.8). However, for the case of second order differencing (Panels a to c of Fig. 5.14), the first rotor to develop in the $\Delta t_s = \Delta t_a$ simulations is more intense and the second rotor somewhat underdeveloped at t = 900 s compared to the coresponding simulations with $\Delta t_s = 1\,s$, $\Delta t_a = 0.1\,s$ (Panel b of Fig. 5.6).

- The third rotor in the t = 900 s solution obtained with fourth order differencing and $\Delta t_s = \Delta t_a = 1\,s$ (Panel d of Fig. 5.14) is better developed than in the corresponding solution obtained with second order differencing (Panel b of Fig. 5.14). In fact, the time-evolution of the three rotors depicted in Fig. 5.14 Panel d, obtained with the fourth order discretization, is very similar to the corresponding simulation obtained with $\Delta t_s = 1\,s$, $\Delta t_a = 0.1\,s$ (Panel b of Fig. 5.8). This illlustrates that the fourth order differencing scheme provides more accurate results than second order differencing at large time-steps (in simulations with second order differencing at relatively large time-steps the time evolution of the three rotors are somewhat different compared to the corresponding simulations performed with smaller adjustment time-steps).

- It may be said that the split semi-Lagrangian scheme, for both second and fourth order differencing applied in the adjustment step, produces very reasonable results at large adjustment time-steps $\Delta t_a = \Delta t_s$. The adjustment time-steps used here are considerably larger than the "sound wave time-steps" used in the corresponding cold bubble solutions shown by Gallus and Rancic (1996), Janjic et al. (2001) and Straka et al. (1993).

In order to investigate the maximum time-steps allowed during the semi-Lagrangian advection step, a second set of experiments was performed. In these experiments the adjustment time-step was kept fixed at $\Delta t_a = 0.5\,s$, but the advection time-step Δt_s was increased in increments of 0.5 until the numerical stability was

Table 5.7: Advection time-step stability experiments, with $\Delta t_a = 0.5$, for various simulations as described in the text.

Differencing and Filtering		TA	TB	TC	TD
SO	Δt_{smax}	1.5	1.5	1.5	Unstable
	HC	0.62	0.62	0.63	-
	VC	0.40	0.43	0.48	-
SH	Δt_{smax}	3.0	3.0	3.0	2.5
	HC	1.20	1.21	1.21	1.03
	VC	0.74	0.77	0.82	0.74
FH	Δt_{smax}	2.0	2.0	2.0	1.5
	HC	0.79	0.79	0.80	0.81
	VC	0.51	0.53	0.56	0.65

destroyed within the 900 s integration period. The maxiumum advection time-step for which numerical stability is maintained is denoted by Δt_{smax}. The experimental settings and notation in Table 5.7 are as described for Table 5.6. In the SH and FH simulations, the Shapiro filter was applied after each adjustment time-step.

A few conclusions can be made from considering the stability experiments presented in Table 5.7:

- the split semi-Lagrangian scheme employing second order differencing in the adjustment step, but without application of the Shapiro filter (simulations SO), is unstable when no explicit diffusion is applied. It is stable at advection Courant numbers as large as about 0.62, for the cases where explicit diffusion is used;

- the split semi-Lagrangian scheme employing second order differencing in the adjustment step, with application of the Shapiro filter after each adjustment time-step (simulations SH) is stable at advection Courant numbers as large as 1.2, provided that explicit diffusion is used. Even for the case of zero diffusion, the scheme is stable at Courant numbers slightly larger than unity. Application of the Shapiro filter, and the associated removal of two-grid-interval waves and noise from the grid, clearly allows the use of significantly larger advection time-steps compared to the SO simulations;

- the split semi-Lagrangian scheme employing fourth order differencing in the adjustment step, with application of the Shapiro filter after each adjustment time-step (simulations SH), is stable for Courant numbers as large as about 0.8. The semi-Lagrangian advection procedure is unconditionally stable for the case of linear advection (see Chapter 4). For fourth

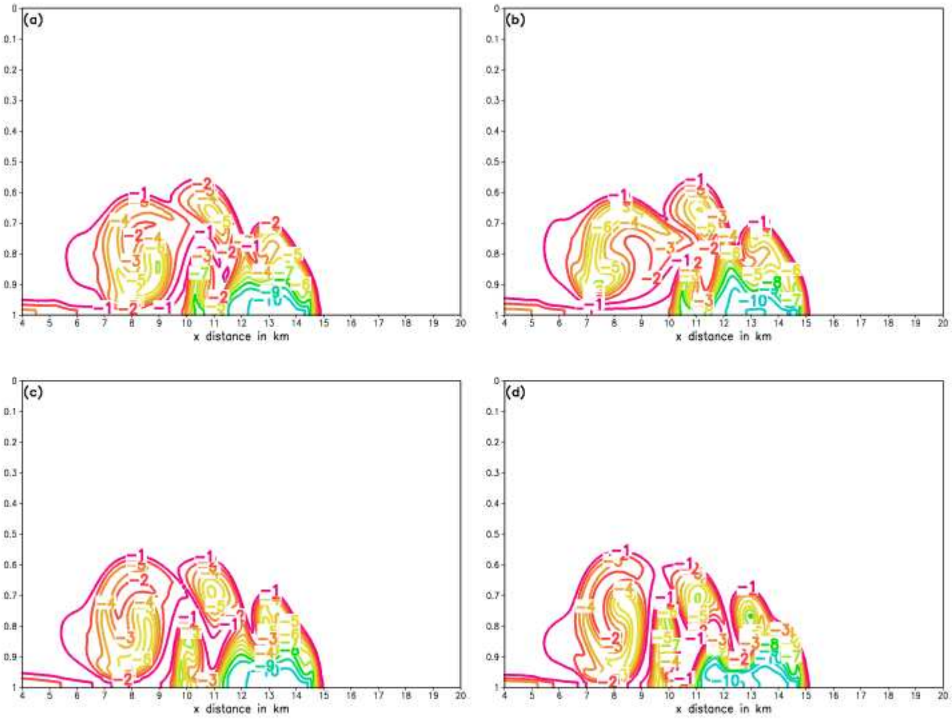

Figure 5.15: The potential temperature deviation after 900 s for the cold bubble test, in the right-hand part of the integration domain, for $0 \leq \sigma \leq 1$: (a) SH simulation with $\Delta t_s = 2\,s$, $\Delta t_a = 0.5\,s$ and $K_s = 50\,m^2s^{-1}$; (b) SH simulation with $\Delta t_s = 3\,s$, $\Delta t_a = 0.5\,s$ and $K_s = 50\,m^2s^{-1}$; (c) FH simulation with $\Delta t_s = 2\,s$, $\Delta t_a = 0.5\,s$ and $K_s = 50\,m^2s^{-1}$; (d) FH simulation with $\Delta t_s = 2\,s$, $\Delta t_a = 0.5\,s$ and $K_s = 25\,m^2s^{-1}$. The Shapiro filter with $p = 4$ was used . The contour interval is 1K.

> order differencing the gravity wave phase speed is simulated more accurately with less retardation than in the case of second order differencing. Thus, the instabilities observed at relatively large advection Courant numbers may possibly be attributed to nonlinear instability that develops in association with these relatively fast moving gravity waves that are not sufficiently controlled by the Shapiro filter at the shortest resolvable scales.

Some of the t = 900 s solutions obtained using large advection time-steps are displayed in Fig. 5.15. Panels a and b show the potential temperature perturbation obtained using second order spatial diferencing, with application of the Shapiro filter at each adjustment time-step (numerical design SH), for advection time-steps of $\Delta t_s = 2\,s$ and $\Delta t_s = 3\,s$ respectively. $K_s = 50\,m^2s^{-1}$ for these simulations. Panel c and d show solutions obtained using fourth order spatial differencing (numerical design FH) with $\Delta t_s = 2\,s$. The diffusion coefficients used to obtain the simulations in Panels c and d are $K_s = 50\,m^2s^{-1}$ and $K_s = 25\,m^2s^{-1}$ respectively.

A few conclusions may be drawn from considering the results displayed in Fig. 5.15:

- even at advection time-steps as large as 2.5 s, the solutions contain the basic flow features, namely the development of three rotors by t = 900 s.
- The gust front has progressed a distance of about 15 km by t = 900 s in all the simulations, which is in close agreement with the simulations obtained using $\Delta t_s = 1\,s$ and $\Delta t_a = 0.1\,s$ (see sections 5.2.5 and 5.2.6). This result confirms that the somewhat slower progress of the gust front in the simulations with $\Delta t_s = \Delta t_a$ (see Fig. 5.14) is caused by the damping induced by the bicubic interpolation scheme during each time-step of the model, and not by the size of the time-steps. In the present simulations (Fig. 5.7), the gravity waves are less damped by the relatively infrequent application of the bicubic interpolation procedure. Thus, a ratio of $\Delta t_s/\Delta t_a$ larger than unity is recommended for application of the split semi-Lagrangian procedure.
- In the simulations where fourth order differencing is used (Panels c and d of Fig. 5.7), the third rotor is better developed than in the second order solutions (Panels a and b of Fig. 5.7). The potential temperature perturbation field for the case $K_s = 25\,m^2s^{-1}$ and mixed second-fourth order differencing, even shows signs of a fourth rotor starting to impact on the leading edge of the gust front.

Overall, it may be said that the split semi-Lagrangian solution procedure is stable and quite accurate at large adjustment and advection time-steps (that is, at large Courant numbers). The good stability properties of the split semi-Lagrangian solution procedure stem from the semi-Lagrangian approach used for the advection terms, and the quasi-elastic nature of the equations.

5.2.10 Efficiency of the elliptic solver

Solving the elliptic equation at the end of each adjustment time-step, represents a fundamental contribution to the number of computations performed in the split semi-Lagrangian solution procedure. In this section, the efficiency of the second and fourth order elliptic solvers described in sections 4.6 and 5.2.6 are quantified for the case of the cold bubble test. Table 5.8 shows the number of iterations required per second of integration time, for various of the experiments conducted in previous sections. Rows SO, SH and FH represent respectively simulations obtained by using second order differencing without application of the Shapiro filter, second order differencing with application of the Shapiro filter after the $\mathrm{N_{th}}$ adjustment time-step, and fourth order differencing with application

Table 5.8: Efficiency of the second and fourth order elliptic solvers, giving the amount of iterations required for convergence per second of integration time, for various simulations as described in the text.

Simulation	EA	EB	EC	ED	ET1	ET2	ER1	ER2
SO	93.6	101.2	114.1	165.7	32.1	53.3	117.2	81.6
SH	91.3	98.6	110.3	129.2	31.4	57.9	104.4	88.4
FH	92.2	98.3	108.8	123.0	31.9	59.2	105.4	97.2

of the Shapiro filter after the $\mathrm{N_{th}}$ adjustment time-step. The explicit diffusion applied along the x and σ axis is as described in section 5.2.4. Columns EA to ED represent simulations obtained with diffusion coefficients of respectively $K_s = 75\,m^2s^{-1}$, $K_s = 50\,m^2s^{-1}$, $K_s = 25\,m^2s^{-1}$ and $K_s = 0\,m^2s^{-1}$. These experiments were performed at 100 m resolution with time-steps $\Delta t_s = 1\,s$ and $\Delta t_a = 0.1\,s$, and are described in sections 5.2.4 (SO), 5.2.5 (SH) and 5.2.6 (FH). The simulations represented by columns ET1 and ET2 were also perfomed at 100 m resolution, but with $\Delta t_s = \Delta t_s = 1\,s$ (ET1) and $\Delta t_s = 1.5\,s$, $\Delta t_a = 0.5\,s$ (ET2). $K_s = 50\,m^2s^{-1}$ for these experiments (which are described in section 5.2.8). The last two columns in Table 5.8, are from the low resolution experiments described in section 5.2.7. Column ER1 represents the 200 m simulations performed with time-steps $\Delta t_s = 2\,s$, $\Delta t_s = 0.2\,s$, whilst column ER2 represents the 400 m simulations obtained with time-steps $\Delta t_s = 4\,s$, $\Delta t_a = 0.4\,s$. $K_s = 50\,m^2s^{-1}$, and fourth order differencing was used to discretize the spatial derivatives in the adjustment step equations for the low resolution experiments discussed here.

From the results shown in Table 5.8, the following conclusions may be drawn:

- The number of iterations required for convergence increases as the magnitude of explicit diffusion decreases (compare columns EA to ED for each of the numerical designs SO, SH and FH). This is to be expected, since finer scale structures are described by the simulations that use relatively small magnitudes of explicit diffusion (see sections 5.2.4, 5.2.5 and 5.2.6).
- Comparing the SO and SH simulations for fixed diffusion coefficients, shows that application of the Shapiro filter generally leads to faster convergence of the SOR procedure. This may be attributed to an effective removal of two-grid interval waves and associated noise by the filter. The slow convergence in the case of zero diffusion without application of the Shapiro filter (simulation SO column ED) indicates, in particular, the negative effect of two-grid-interval waves on the eficiency of the elliptic solver. For the relatively large advection time-step simulations (column ET2) and relatively low spatial resolution simulations (column ER2), convergence is

somewhat slower when the filter is applied (compared to the corresponding SO simulations).

- The number of iterations required for the solutions obtained with fourth order differencing (row FH in Table 5.8) is quite similar to the number required in the corresponding solutions obtained with second order differencing (row SH of Table 5.8). In fact, for most of the solutions obtained with $\Delta t_s = 1\,s$, $\Delta t_a = 0.1\,s$ at 100 m resolution, less iterations are required for by fourth order solver than by the second order solver per second of integration time. Thus, the larger amount of grid points used by the fourth order solver compared to the second order solver do not lead to slower convergence iteration wise. Of course, more calculations are performed when the fourth order solver is used (since it makes use of 25 surrounding points for the geopotential calculation at each grid point away from the boundaries, compared to the 9 points needed by the second order solver). In this way, the use of the fourth order solver does slow down the numerical integration process.

- The 200 m grid spacing simulations require slightly more iterations per second of integration time than the corresponding 100 m grid spacing simulations (compare columns EB and ER1). The 400 m solutions require less iterations per second of integration time than the corresponding 200 m and 100 m simulations.

- The simulations employing the time-steps $\Delta t_s = \Delta t_a = 1\,s$ and $t_s = \Delta 1.5\,s$, $\Delta t_a = 0.5\,s$ require significantly less iterations per second of integration time than the corresponding simulations with $\Delta t_s = 1\,s$ and $\Delta t_a = 0.1\,s$ (compare columns ET1, ET2 and EB). Clearly, significant advantages are to be gained in computation time with an increase of particularly the adjustment time-step used in the simulations.

Xue (1989) has developed a FFT procedure to solve the closely related elliptic equation used in the σ coordinate MP model (see section 4.6). It is not clear to what extent this procedure offers computational advantages over the SOR procedure aplied in this study. The procedure of Xue (1989) combines the use of a double Fourier transform, a Gaussian elimination procedure and an iterative technique to solve the ellipctic equation (Xue, 1989; Xue and Thorpe, 1991, also see section 4.6). They found that only “a few” iterations are needed per time-step. However, the time-steps applied in the studies by Xue (1989) and Xue and Thorpe are comparativley smaller to the “1 s of the integration time” over which the iterations are counted in this study . They also do not state explicitly how the number of iterations required depends on the size of the time-step used, however, their explicit solutions were generally performed at Courant numbers much smaller than in the experiments described in the present study (see section 4.2.9). It should also be kept in mind that in addition to the iterative process used in the method of Xue (1989), more calculations are needed for the double Fourier transform and Gaussian elimination that are applied. Still, potential computational advantages of the approach followed by Xue (1989) over the present SOR procedure is worth to be explored (see section 4.6).

5.3 Warm bubble experiments in two spatial dimensions

5.3.1 Design of the warm bubble tests

The warm bubble simulations presented in this section closely follow the experimental design of the two-dimensional simulations performed by Janjic et al. (2001). Similar experiments were performed by Droegemeier (1985), Mendez-Nunez and Carroll (1994) and Gallus and Rancic (1996). In an initially dry, at rest and isentropic atmosphere with potential temperature 300 K, a circularly-shaped initial disturbance is introduced for the potential temperature:

$$\Delta\theta_0(x,z) = 6.6\cos^2(\frac{\pi}{2}r), \tag{5.6}$$

for $r \leq 1$, where $r^2 = \left[(x-x_c)/x_t\right]^2 + \left[(z-z_c)/z_t\right]^2$, $x_c = 0$ m, $z_c = 2750$ m, $x_t = 2500$ m and $z_t = 2500$ m.

The integration domain extends over $-10000\,m \leq x \leq 10000\,m$ in the horizontal. The top of the model domain is chosen to be 135 hPa (about 13500 m). The center of the initial disturbance is in the middle of the domain in the x direction, that is, 10 km away from the lateral boundaries. Unless where stated differently, the horizontal resolution in the following experiments is 100 m, and 135 equally spaced σ levels are used to give a vertical resolution of about 100 m on the average. The bubble simulations of Gallus and Rancic (1996) and Janjic (2001) were performed at similar spatial resolutions, and also employed terrain-following pressure-based coordinates. Mendez-Nunez and Carroll performed corresponding experiments at 500 m resolution, using the fully-elastic z coordinate equations. It may be noted that a different class of warm bubble experiments have been performed at even higher resolutions (10 - 20 m) over much smaller domains using a smaller temperature perturbation (Robert, 1993; Mendez-Nunez and Carroll, 1994; Hsu and Sun, 2001).

5.3.2 A reference solution obtained with fourth order spatial differencing

The numerical settings of the split semi-Lagrangian scheme that were found to give superior results in the cold bubble tests, are used to obtain the reference warm bubble simulation of the present section. In the semi-Lagrangian advection step, the D_3 scheme of McGregor (1993) is used for the calculation of departure points (see Chapter 4 and section 5.2.7). The spatial derivatives in the departure point formula and the term $A^*_{p_s}$ are evaluated using second order spatial differencing. All spatial derivatives in the adjustment step equations are

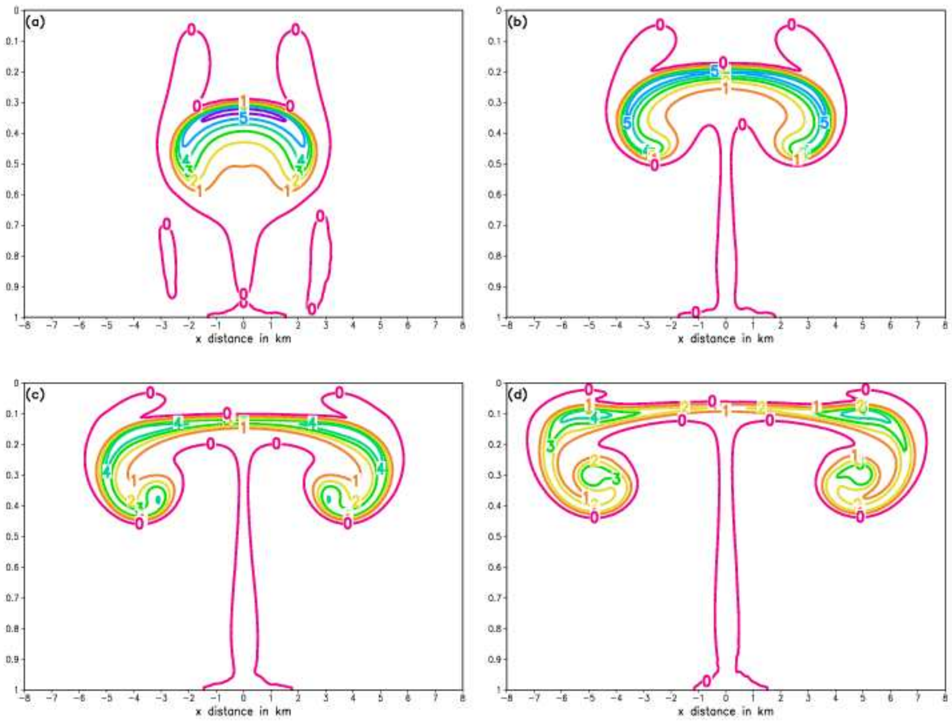

Figure 5.16: Reference solution for the warm bubble test. Potential temperature perturbation for $-8000\,m \leq x \leq 8000\,m$ and $0 \leq \sigma \leq 1$: (a) after 360 s; (b) after 520 s; (c) after 720 s; (d) after 900 s. The contour interval is 1 K.

discretized using fourth order differencing (see Chapter 4 and section 5.2.6). The Shapiro filter is applied with p = 4, with lower order filtering performed near the lateral and vertical boundaries (see Chapter 4 and section 5.2.5).

The values of the diffusion coefficients used in the explicit diffusion step, for diffusion along the x axis, are $K_s = 300\,m^2s^{-1}$ and $K_{Ts} = 50\,m^2s^{-1}$. Similar magnitudes of explicit diffusion are applied along the σ axis, for u and T respectively. That is, $K_\sigma = K_s\left(\Delta\sigma^2/\Delta x^2\right)$ and $K_{T\sigma} = K_{Ts}\left(\Delta\sigma^2/\Delta x^2\right)$, so that the non-dimensional quantity $K\Delta t_s/\Delta n^2$ defined in Chapter 4 has the same magnitude along the x and σ axis, for u and T respectively (see Janjic et al., 2001). The magnitude of explicit diffusion applied to the u field is fairly large, compared to the corresponding magnitudes of explicit diffusion used in the cold bubble tests. The choice of explicit diffusion coefficients used here follows the experimental design of Janjic et al. (2001). In fact, in order to reproduce the basic time evolution of the warm bubble, as discussed in the experiments of Gallus and Rancic (1996) and Janjic et al. (2001), the relatively large diffusion of the u field is necessary. If smaller magnitudes of explicit diffusion are used, finer scale structures of the flow field may be resolved (see the next section). The elliptic equation is solved with SOR, using $rl = 1.6$ as relaxation factor. The solution was found to be sufficiently converged using $\epsilon = 10^{-6}$ as criterion of convergence. On average 16.13 iterations are required per second of integration time over the 900 s integration period, that is, less than 2 iterations per adjustment time-step $t_a = 0.1\,s$ (see row WREF of Table 5.9). The potential temperature deviation $\theta^{'}$ from the isentropic background state after 360, 540, 720 and 900 s is shown in Fig. 5.16. The contour interval is 1 K. The corresponding vertical velocity fields $\hat{w}$ are shown in Fig. 5.17, with contour interval 2ms^{-1}.

In Fig. 5.16 it can be seen that that warm bubble is simulated to ascend in the isentropic environment. This occurs in conjunction with an updraft that develops in response to the positive buoyancy associated with the presence of the warm bubble in the colder environment (Fig. 5.17). Since the updraft is the strongest at the center of the bubble, it rises the fastest, causing the potential temperature gradient to steepen in the upper part of the bubble (Fig. 5.16 Panels a and b). By mass conservation, the updraft induces convergence below the vertical velocity maximum, and divergence occurs above the vertical velocity maxiumum. The convergence-divergence pattern results in the formation of two vortices, one on each side of the symmetry axis. As noted in the lower resolution experiments of Mendez-Nunez and Carroll (1994), relatively cooler air from the environment is entrained into the lower part of the bubble by the two rotors (Note the intrusion of the 0 K contour into the lower part of the bubble in Panels b, c and d of Fig. 5.16). The divergent flow associated with the rotors at the uper part of the bubble causes the potential temperature maximum to move away from the center axis. The splitting that occurs in the potential temperature field is visible in the t = 540 s potential temperature deviation field (Panel b of Fig. 5.16), and is well developed in the t = 720 and 900 s fields (Panels c and d of Fig. 5.16). Thus, two potential temperature maxima evolve, one on each side of the symmetry axis.The positive buoyancy associated with these potential temperature maxima, leads to the development of two secondary updrafts (and eventually two secondary rotors) on both sides of the symmetry axis (Panels c and d of Fig. 5.17). A portion of the high potential temperature air is drawn into each main rotor, causing two sub-maxima to be present by t = 900 s on each side of the symmetry axis, within each of the main rotors.

The rate of ascent and the intensity of the disturbance shown in Fig. 5.16 agree with those reported by Gallus and Rancic (1996) and Janjic (2001) (Note that the present results are displayed in a $x - \sigma$ coordinate system, whilst the mentioned autors display their results in an $x - z$ coordinate system). The time-evolution of the main flow features (the development of the rotors and the formation of a potential temperature maximum on each side of the symmetry axis) are also similar for the various simulations.

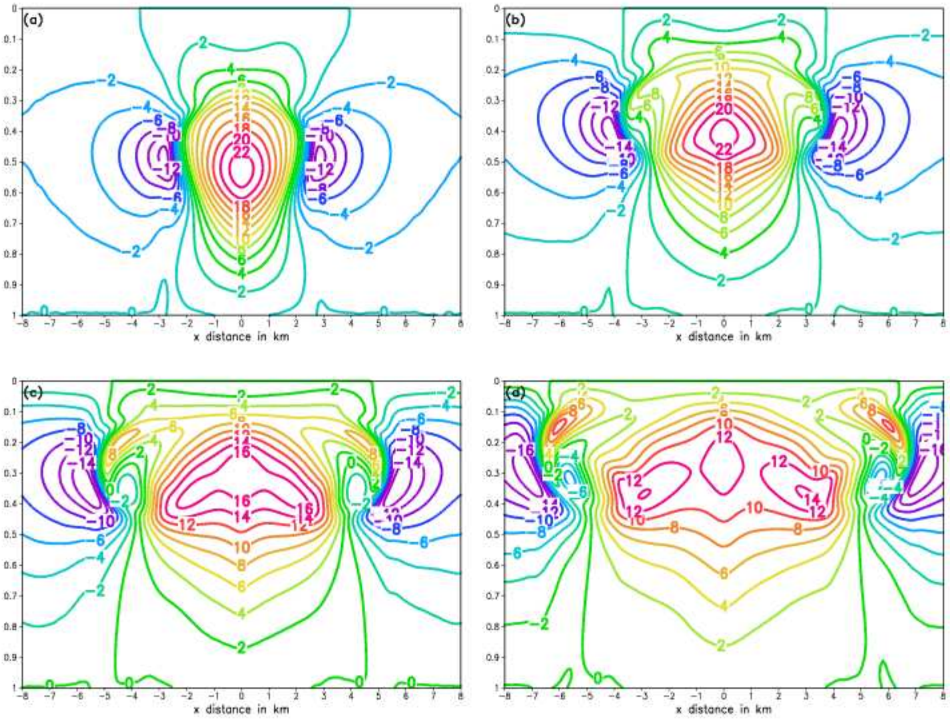

Figure 5.17: Reference solution for the warm bubble test. Vertical velocity $\hat{w}$ for $-8000\,m \leq x \leq 8000\,m$ and $0 \leq \sigma \leq 1$: (a) after 360 s; (b) after 520 s; (c) after 720 s; (d) after 900 s. The contour interval is 2 ms^{-1}.

The horizontal and vertical velocities u and $\hat{w}$ attains maximum values of $u_{max} = 16.37$ and $w_{max} = 24.20\,ms^{-1}$during the 900 s integration period, respectively. The corresponding maximum values of the horizontal and vertical advection Courant numbers attained (see Chapter 4) are 0.16 and 0.29, respectively (see row WREF of Table 5.9). The simulations by Gallus and Rancic (1994) were performed using a sound wave time-step of less than 0.09 s, and an advection time-step of double the sound-wave time-step. The experiments by Janjic et al. (2001) were performed using a time-step of 0.3 s. Thus, the advection time-step $\Delta t_s = 1\,s$ used in the present study is considerably larger than the time-steps used in the studies by the mentioned authors. The simulations depicted in Figs. 5.16 and 5.17 are smooth and without any signs of two-grid-interval noise. This indicates the application of the Shapiro filter, and the additional damping that result from the bicubic interpolation and explicit diffusion, effectively removes the two-grid-interval waves from the nonstaggered grid. In fact, the split semi-Lagrangian scheme produces stable and smooth warm bubble solutions at much larger time-steps $\Delta t_s$and Δt_a, with larger associated Courant numbers (see section 5.3.4).

5.3.3 Marginally and poorly resolved flow

In this section, lower resolution warm bubble experiments are performed, in order to investigate the performance of the split semi-Lagrangian scheme for the case of flow that is marginally or poorly resolved. Corresponding cold bubble tests were carried out in section 5.2.8. As mentioned earlier, operational constaints are likely to limit the application of nonhydrostatic models to NWP and climate simulation to resolutions where the flow is only marginally or even poorly resolved (see Chapter 1 and section 5.2.8).

The experiments performed in the present section closely follow the experimental design used to obtain the reference solution. The only differences are with respect to the time-steps, spatial resolutions and explicit diffusion coefficients that are used. Some details of the simulations are listed in Table 5.9. In the first two experiments performed, the horizontal resolution is 200 m, and 68 equally spaced σ levels are used to give a vertical resolution of about 200 m on the average. The time-steps used are $\Delta t_s = 2\,s$, $\Delta t_a = 0.2\,s$. In the first experiment (see row WM of Table 5.9), $K_s = 300\,m^2s^{-1}$ and $K_{Ts} = 50\,m^2s^{-1}$. Diffusion of similar magnitudes is applied along the σ axis, for u and T respectively (see the previous section). Thus, the explicit diffusion coefficients used in this experiment are exactly the same as for the reference warm buble experiment, however, the nondimensional quantity $K\Delta t_s/\Delta n^2$ (see Chapter 4) is two times smaller with respect to the value it assumes in the reference solution. The 200 m simulation may be therefore be expected to be less diffused than the reference simulation. In the second 200 m simulation performed (row WMD of Table 5.9), the diffusion coefficients used are $K_s = 600\,m^2s^{-1}$ and $K_{Ts} = 100\,m^2s^{-1}$. Diffusion of similar magnitudes is applied along the σaxis, for u and T respectively. Thus, for this simulation the non-dimensional quantity $K\Delta t_s/\Delta n^2$ has the same value

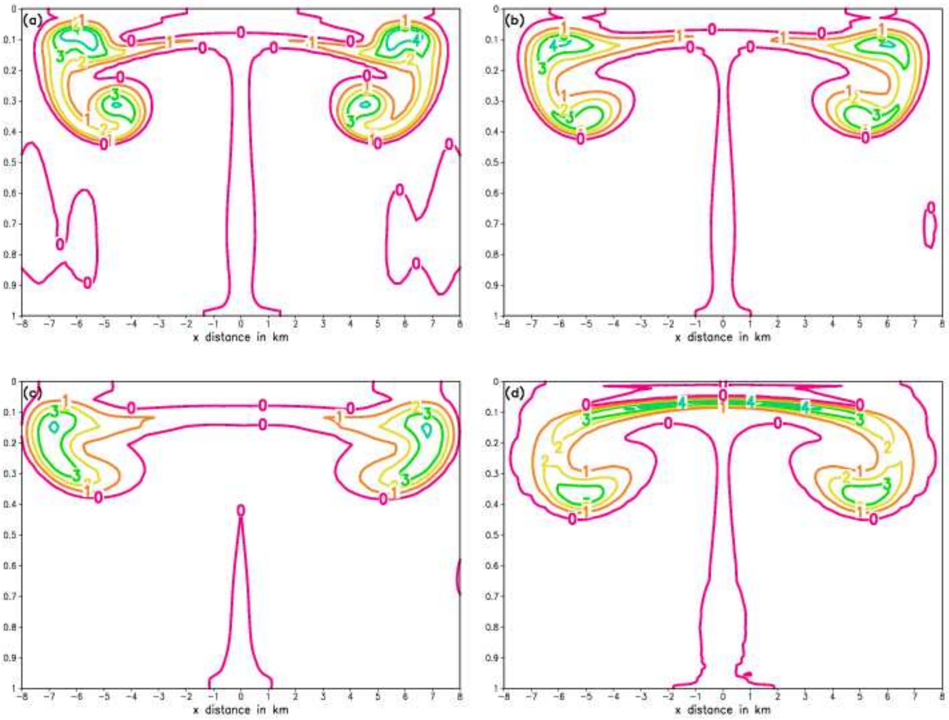

Figure 5.18: Marginally and poorly resolved flow in the warm bubble test. The potential temperature deviation after 900 s, for $-8000\,m \leq x \leq 8000\,m$ and $0 \leq \sigma \leq 1$: (a) $\Delta z \approx \Delta x = 200\,m$ with $K_s = 300\,m^2 s^{-1}$ and $K_{Ts} = 50\,m^2 s^{-1}$;(b) $\Delta z \approx \Delta x = 200\,m$ with $K_s = 600\,m^2 s^{-1}$ and $K_{Ts} = 100\,m^2 s^{-1}$; (c) $\Delta z \approx \Delta x = 400\,m$ with $K_s = 1200\,m^2 s^{-1}$ and $K_{Ts} = 200\,m^2 s^{-1}$; (d) $\Delta z \approx 100\,m$, $\Delta x = 500\,m$ with $K_s = 300\,m^2 s^{-1}$ and $K_{Ts} = 50\,m^2 s^{-1}$. The contour interval is 1 K.

as for the reference simulation, and it may be expected to be similarly diffused. The third simulation is performed using a horizontal resolution of 400 m, and 35 equally spaced σlevels are used to give a resolution of about 400 m in the vertical, on the average (see row WP of Table 5.9). The time-steps used are $\Delta t_s = 4\,s$, $\Delta t_a = 0.4\,s$. The diffusion coefficients used are $K_s = 1200\,m^2s^{-1}$ and $K_{Ts} = 200\,m^2s^{-1}$, with diffusion of similar magnitudes applied along the σ axis, for u and T respectively. In the final experiment performed in this section, the horizontal resolution is 500 m, and 135 σ levels are used as in the reference simulation (row WPM of Table 5.9). The time-steps Δt_s and Δt_a and the explicit diffusion used are as specified for the reference simulation. The potential temperature deviation $\theta^{'}$ fields obtained for the various experiments, at t = 900 s, are shown in Fig. 5.18. The corresponding vertical velocity $\hat{w}$ fields are shown in Fig. 5.19.

A few remarks can be made with regard to the various t = 900 s solutions displayed in Figs. 5.18 and 5.19.

- The 200 m solution obtained with with $K_s = 300\,m^2s^{-1}$ and $K_{Ts} = 50\,m^2s^{-1}$ (Panels a of Figs. 5.18 and 5.13) is less diffused than the corresponding 100 m solution (Panels d of Figs. 5.16 and 5.17) and the 200 m solution obtained with $K_s = 600\,m^2s^{-1}$ and $K_{Ts} = 100\,m^2s^{-1}$ (Panels b of Figs. 5.12 and 5.19). This is most evident from the evolution of the potential temperature pattern by t = 900 s, as shown in Panel a of Fig. 5.18). For the relatively less diffused solution, the buoyancy of the potential temperature maxima on both sides of the symmetry axis has overcome the horizontal momentum provided by the rotors. In stead of moving largely sideways as in the more diffused simulations, the maxima shows a clear vertical displacement by t = 900 s. This vertical displacement is related to the development of two intense secondary updrafts, one on each side of the symmetry axis (Panel a of Fig. 5.19). These secondary updrafts are also present in the more diffused simulations, but are less intense (Panel d of Fig. 5.17 and Panel b of Fig. 5.19). The vertical displacement of the potential temperature maxima are also present in in 100 m solutions (not shown) obtained with diffusion coefficients having half the magnitude (or smaller) of those used to obtain the reference solution.

- For the relatively less diffused 200 m simulation, the a convergence criterion $\epsilon = 10^{-6}/2$ needs to be used to obtain a sufficiently converged solution. This is to be expected, since the relatively less diffused solution contains some finer scale and more intense structures than in the more diffused cases.

- The 400 m solution shown for t = 900 s (Panels c of Figs. 5.18 and 5.13) was obtained using explicit diffusion comparable to that used to obtain the reference solution. It shows the development of the main flow features, namely one rotor on each side of the symmetry axis. Potential temperature maxima are simulated to be present on both sides of the symmetry axis, although the detail of two separated submaxima within the rotors (as in the higher resolution simulations) are not present. The development of two secondary updrafts are present in the 400 m solution for t = 900 s, although the two secondary rotors are not fully developed by this time.

- The evolution of the potential temperature perturbation field by t = 900 s obtained with $\Delta x = 500\,m$, $\Delta z \approx 100\,m$ (5.18) is similar to that of the reference solution. Potential temperature sub-maxima occur within each of the two main rotors. The main potential temperature maxima on either sides of the symmetry axis are not well developed, however. This is related to the fact that the secondary updrafts are only starting to evolve by t = 900 s (Panle d of Fig. 5.19).
- All the $\theta^{'}$ and $\hat{w}$ fields shown are smooth and without any signs of numerical noise. It may be said that as in the corresponding cold bubble tests (section 5.2.8), the split semi-Lagrangian scheme functions well for the cases of marginally and poorly resolved flow.

5.3.4 Time-step experiments and stability

In this section, time-step and stability tests are performed, similar to those described in section 5.2.9 for the cold bubble tests. The resolution and general design of the experiments described in this section are as for the reference solution (see section 5.3.2). The only differences are with respect to the size of the time-steps, the criterion of convergence ϵ used and the frequency of application of the Shapiro filter. In the first set of experiments, $\Delta t_s = \Delta t_a$. The split semi-Lagrangian scheme is stable over the 900 s integration period for time-steps as large as 1.5 s (with application of the Shapiro filter after each adjustment time-step). However, for the solution to be fully converged using time-steps $\Delta t_s = \Delta t_a$ this large, a criterion of convergence $\epsilon = 10^{-6}/3$ needs to be used. In the second set of experiments performed, the adjustment time-step was kept fixed as $\Delta t_a = 0.5\,s$, and the Shapiro filter was applied after each adjustment step. Here it was found that the semi-Lagrangian scheme is unconditionally stable, and only accuracy requirements place a limit on the maximum time-step Δt_s to be used. The criterion of convergence $\epsilon = 2.10^{-6}/3\,s$ is sufficient for convergence of the $\Delta t_a = 0.5\,s$ tests.

Some of the t = 900 s solutions obtained using large time-steps are displayed in Figs. 5.20 (potential temperature perturbation $\theta^{'}$) and 5.21 (vertical velocity $\hat{w}$). Panels a to d of Figs. 5.20 and 5.21 represent solutions obtained with time-steps $\Delta t_s = \Delta t_a = 0.5\,s$, $\Delta t_s = \Delta t_a = 1.5\,s$, $\Delta t_s = 2.5\,s$, $\Delta t_a = 0.5\,s$ and $\Delta t_s = 5\,s$, $\Delta t_a = 0.5\,s$, respectively. Some details of the simulations may be found in Table 5.9.

A few remarks can be made with regard to the various t = 900 s solutions displayed in Figs. 5.20 and 5.21.

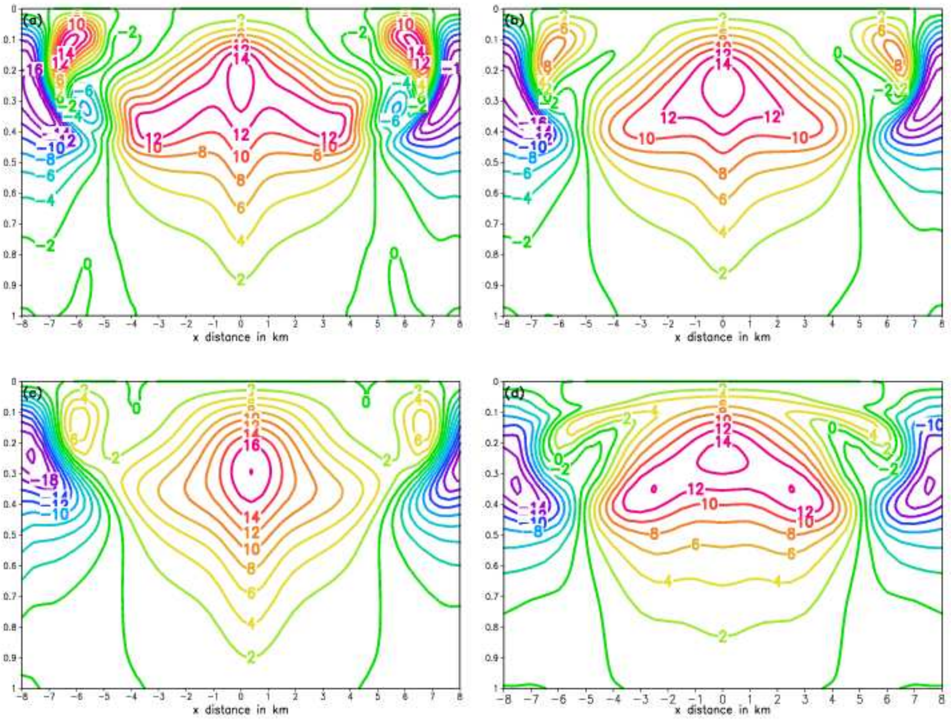

Figure 5.19: Marginally and poorly resolved flow in the warm bubble test. The $\hat{w}$ component of the wind after 900 s, for $-8000\,m \leq x \leq 8000\,m$ and $0 \leq \sigma \leq 1$: (a) $\Delta z \approx \Delta x = 200\,m$ with $K_s = 300\,m^2 s^{-1}$ and $K_{Ts} = 50\,m^2 s^{-1}$;(b) $\Delta z \approx \Delta x = 200\,m$ with $K_s = 600\,m^2 s^{-1}$ and $K_{Ts} = 100\,m^2 s^{-1}$; (c) $\Delta z \approx \Delta x = 400\,m$ with $K_s = 1200\,m^2 s^{-1}$ and $K_{Ts} = 200\,m^2 s^{-1}$; (d) $\Delta z \approx 100\,m$, $\Delta x = 500\,m$ with $K_s = 300\,m^2 s^{-1}$ and $K_{Ts} = 50\,m^2 s^{-1}$. The contour interval is 2ms^{-1}.

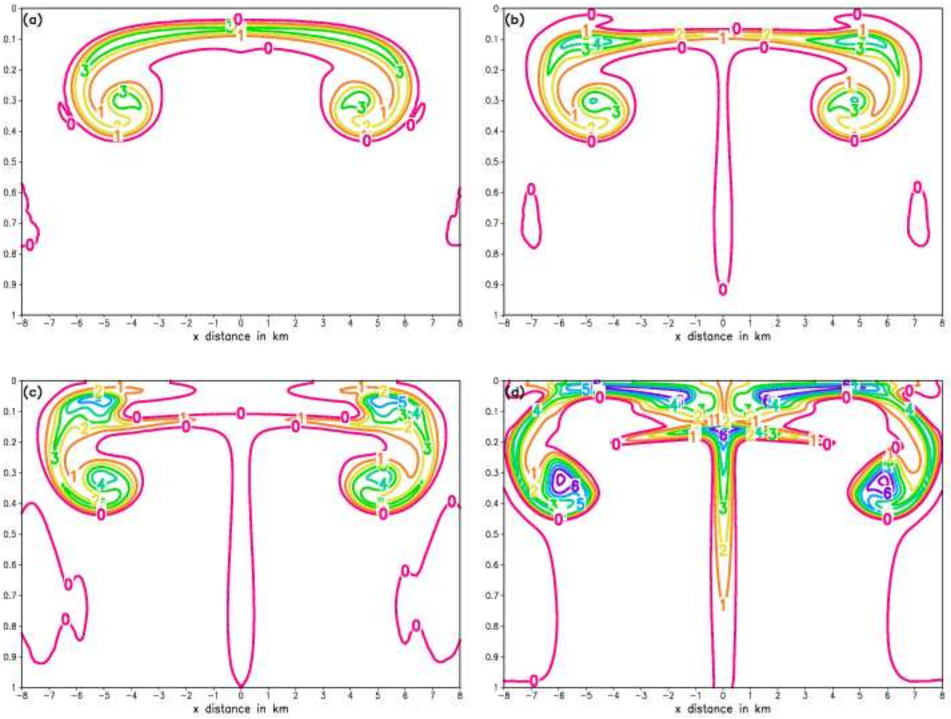

Figure 5.20: The potential temperature deviation after 900 s for the warm bubble test, for $-8000\,m \leq x \leq 8000\,m$ and $0 \leq \sigma \leq 1$: (a) $\Delta t_s = \Delta t_a = 1.5\,s$; (b) $\Delta t_s = 1.5\,s$, $\Delta t_a = 0.5\,s$(c) $\Delta t_s = 2.5\,s$, $\Delta t_a = 0.5\,s$; (d) $\Delta t_s = 5\,s$, $\Delta t_a = 0.5\,s$. The contour interval is 1K.

- For the simulation obtained with $\Delta t_s = \Delta t_a = 1.5\,s$, the evolution of the main flow features and the rate of ascent of the bubble correspond to that of the reference solution (Fig. 5.16). However, the t = 900 s solution is slightly diffused compared to the refence solution, and the splitting of the potential temperature field into maxima on both sides of the symmetry axis is not as well defined (compare Panel a of Fig. 5.20 to Panel d of Fig. 5.16). This latter is related to the relatively less well developed secondary updrafts simulated for the $\Delta t_s = \Delta t_a = 1.5\,s$ solution (Panel a of Fig. 5.17).

- The diffused nature of the $\Delta t_s = \Delta t_a = 0.5\,s$ solutions may be attributed to the damping that results from the bicubic interpolations performed during each time-step. For simulations where the adjustment time-step is less than the advection time-step, flow features can develop more unhindered by the damping of the semi-Lagrangian advection scheme. This is confirmed when the t = 900 s solution obtained with $\Delta t_s = 1.5\,s$, $\Delta t_a = 0.5\,s$ is considered (Panels b of Figs. 5.20 and 5.21) This solution resembles the reference solution very closely. Two well developed potential temperature maxima are present, one of each side of the symmetry axis (Panel b of Fig. 5.20). These have resulted in the formation of two well developed secondary updrafts (5.21). The latter are starting to impact on the flow field, resulting in a slight vertical displacement of the potential temperature maxima by t = 900 s. Similar results have been obtained in the cold bubble tests with regard to the damping effect of the bicubic interpolations.

- For the t = 900 s solution obtained with $\Delta t_s = 2.5\,s$, $\Delta t_a = 0.5\,s$, the two potential temperature maxima are displaced further in the vertical than in the reference solution (compare Panel c of Fig. 5.20 to Panel d of Fig. 5.16). With the more infrequent application of bicubic interpolation and explicit diffusion in this simulation, the flow features are less damped. The positive buoyancy associated with the relatively intense potential temperature maxima (compared to the reference solution), has resulted in the formation of two intense secondary updrafts (Panel c of Fig. 5.21). These, in return, are responsible for the stronger vertical displacement of the potential temperature maxima. The maximum horizontal and vertical Courant numbers attained in the simulation with $\Delta t_s = 2.5\,s$ are 0.43 and 0.72, respectively (see Table 5.9).

- The split semi-Lagrangian scheme is stable at even larger advection time-steps. The t = 900 s solution shown in Panels d of Figs. 5.20 and 5.21 was obtained with time-steps $\Delta t_s = 5\,s$, $t_a = 0.5\,s$. The maximum horizontal and vertical advection Courant numbers attained are 1.19 and 1.51, respectively (see Table 5.9). However, although stable, the t = 900 solution for the vertical velocity $\hat{w}$ is noisy (Panel d of Fig. 5.21). The secondary updrafts are very intense and have displaced the potential temperature maxima to the top of the model atmosphere (Panel d of Fig. 5.20).

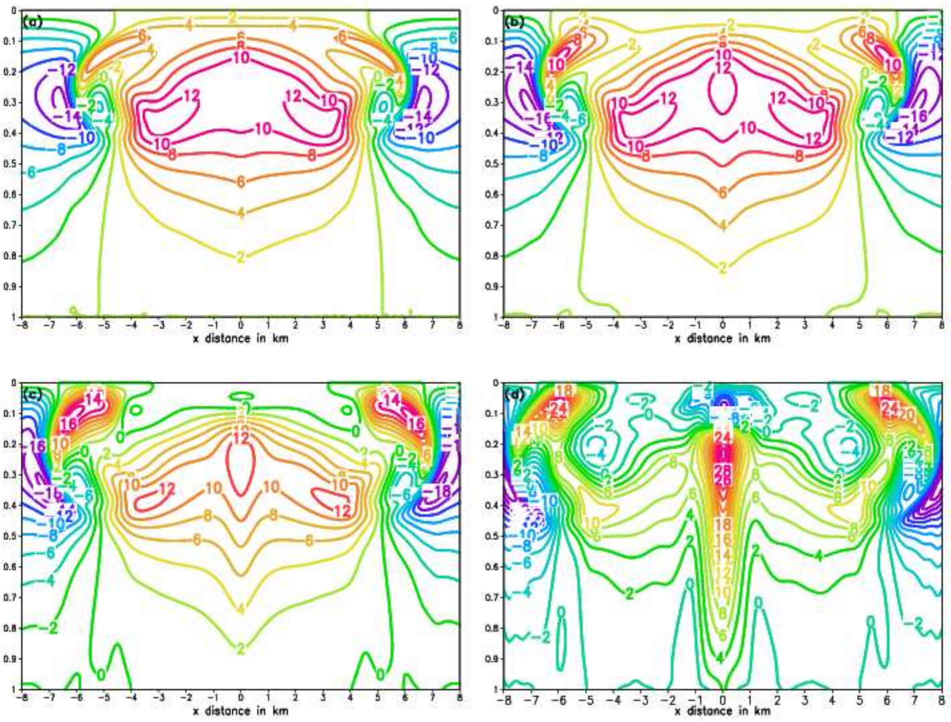

Figure 5.21: The vertical component of the velocity field $\hat{w}$ after 900 s for the warm bubble test, for $-8000\,m \leq x \leq 8000\,m$ and $0 \leq \sigma \leq 1$: (a) $\Delta t_s = \Delta t_a = 1.5\,s$; (b) $\Delta t_s = 1.5\,s$, $\Delta t_a = 0.5\,s$(c) $\Delta t_s = 2.5\,s$, $\Delta t_a = 0.5\,s$; (d) $\Delta t_s = 5\,s$, $\Delta t_a = 0.5\,s$. The contour interval is 2ms^{-1}.

- The t = 900 s solutions shown in Figs. have been obtained using advection and adjustment time-steps much larger than in the corresponding solutions shown by Gallus and Rancic (1994) and Janjic et al. (2001). In fact, for the warm bubble test the size of the advection time-step used is solely determined by accuracy considerations, since the split semi-Lagrangian scheme was found to be unconditionally stable. In the case of the cold bubble tests, the split semi-Lagrangian scheme became unstable at Courant numbers larger than about 0.8. This suggests than the non-linear instability has a more important effect in the cold bubble test, where more intense and finer scale features are present than in the warm bubble simulations described here.

5.3.5 Efficiency of the elliptic solver

The number of iterations required per second of integration time, for each of the various simulations discussed in the previous sections, is listed in Table 5.9. For the simulations which are less diffused, either because of the smallness of the nondimensional quantity $K\Delta t_s/\Delta n^2$ or because of the infrequent application of explicit diffusion and bicubic interpolations, a criterion of convergence $\epsilon < 10^{-6}$ is required for the solution to be sufficiently converged (see Table 5.9). The following conclusions may be drawn based on the results in Table 5.9.

- For sufficient convergence of the reference solution, less than 20 iterations are required per second of integration time, that is, less than 2 iterations per adjustment time-step of 0.1 s (row WREF).
- The simulations that are similarly diffused (damped) as the reference solution generally require about 20 iterations per second of integration time (rows WMD, WPM and WT1).
- Simulations that are less diffused than the reference solution contain finer scale structures and more iterations per second of integration time for sufficient convergence. There are mainly three effects (possibly working in combination) that result in simulations to be less diffused:

1. Smallness of the non-dimensional quantity $K\Delta t_s/\Delta n^2$ (row WM).
2. The infrequent application of the bicubic interpolation scheme when large advection time-steps are used (rows WP, WT3 and WT4).
3. The use of relatively large advection time-steps in combination with smaller adjustment time-steps (rows WT2, WT3 and WT4).

- The relaxation factor $w_s = 1.6$ was found to lead to the fastest convergence of the SOR procedure in the warm bubble tests performed. In the cold bubble tests, $w_s = 1.9$ is the optimum value.
- The warm bubble tests generally require significantly fewer iterations per second of integration time than the cold bubble tests. This is due to the finer scale structures that are present in the less diffused cold bubble tests.
- Recalling the discussion on the efficiency of the elliptic solver for the cold bubble test and the comparative efficiency of the method of Xue (1989), it may be said that the SOR procedure provides efficient solutions for the case of the warm bubble test.

5.4 A cold bubble experiment in three spatial dimensions

5.4.1 Design of the three-dimensional cold bubble test

The experiment described in this section is an extension to three spatial dimensions of the two-dimensional cold bubble downburst problem described in

Table 5.9: Experimental design, maximum horizontal (HC) and vertical (VC) advection Courant numbers, criterion of convergence ϵ and average number of iterations per second of integration time, for various of the simulations as described in the text.

Simulation	Δx	$\Delta z \approx$	Δt_s	Δt_s	HC	VC	ϵ	Iterations
WREF	100	100	1	0.1	0.16	0.29	10^{-6}	16.13
WM	200	200	2	0.2	0.18	0.29	$10^{-6}/2$	54.99
WMD	200	200	2	0.2	0.15	0.28	10^{-6}	22.59
WP	400	400	4	0.4	0.16	0.25	10^{-6}	43.81
WPM	500	100	1	0.1	0.03	0.27	10^{-6}	19.25
WT1	100	100	1.5	1.5	0.22	0.41	$10^{-6}/3$	17.92
WT2	100	100	1.5	0.5	0.23	0.42	$2.10^{-3}/3$	26.15
WT3	100	100	2.5	0.5	0.43	0.72	$2.10^{-6}/3$	26.98
WT4	100	100	5	0.5	1.19	1.51	$2.10^{-6}/3$	36.65

section 5.2.1. In an initially dry, at rest and isentropic atmosphere with potential temperature 300 K, an ellipsoidally-shaped initial disturbance is introduced for the temperature:

$$\Delta T_0(x,z) = -15\cos^2(\frac{\pi}{2}r), \tag{5.7}$$

for $r \leq 1$, where, $r^2 = [(x - x_c)/x_t]^2 + [(y - y_c)/y_t]^2 + [(z - z_c)/z_t]^2$, $x_c = y_c = 0$ m, $z_c = 3000$ m, $x_t = y_t = 4000$ m and $z_t = 2000$ m.

The integration domain extends over $-20000\,m \leq x \leq 20000\,m$ and $-20000\,m \leq y \leq 20000\,m$ in the horizontal. The top of the model domain is chosen to be 442 hPa (about 6400 m). The center of the initial disturbance is in the middle of the horizontal domain, that is, 20 km away from any of the lateral boundaries. The horizontal resolution used in the present experiment is 500 m, and 65 equally spaced σ levels are used to give a vertical resolution of about 100 m on the average. The experiment corresponds to the two-dimensional cold bubble experiment PM described in section 5.2.8, which was performed at the same horizontal and vertical resolutions.

5.4.2 A three-dimensional cold bubble simulation obtained with fourth order differencing

The numerical settings of the split semi-Lagrangian scheme that were found to give optimum results in the two-dimensional convective bubble tests are used to perform the three-dimensional cold bubble simulation. In the semi-Lagrangian

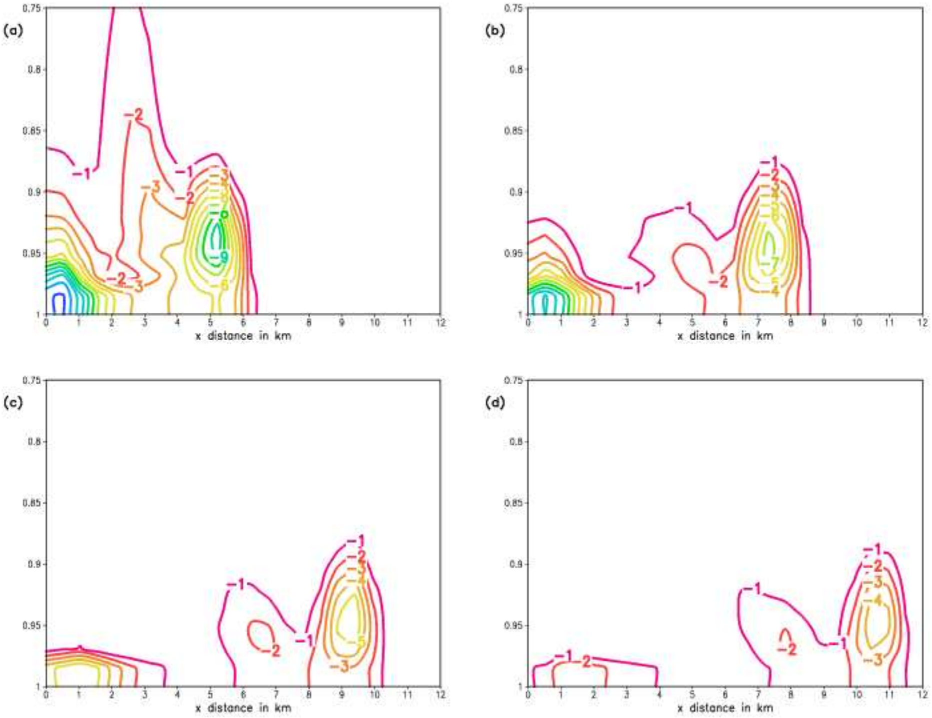

Figure 5.22: The three-dimensional cold bubble test. Vertical cross section of the potential temperature perturbation at $y = 0$, for $0\,m \leq x \leq 12\,000\,m$ and $0.75 \leq \sigma \leq 1$: (a) after 360 s; (b) after 520 s; (c) after 720 s; (d) after 900 s. The contour interval is 1 K.

advection step, the D_3 scheme of McGregor (1993) is used for the calculation of departure points (see Chapter 4). Note that the departure points are calculated in three spatial dimensions, and that tri-cubic spatial interpolation is used to evaluate the values of variables at the departure points. The spatial derivatives in the departure point formula and the term $A^*_{p_s}$ are evaluated using second order spatial differencing. All spatial derivatives in the adjustment step equations are discretized using fourth order differencing (see Chapter 4). Thus, fourth order differencing is used to discretize all partial derivatives in the three-dimensional elliptic equation **(3.81)**. The Shapiro filter is applied with p = 4, with lower order filtering performed near the lateral and vertical boundaries (see Chapter 4 and section 5.2.5). For each variable, the filter is applied consecutively along the x, y and σ axis (see Chapter 4). The values of the diffusion coefficients used in the explicit diffusion step, for diffusion along the x and y axis, are $K_s = K_{Ts} = 50\, m^2 s^{-1}$. Diffusion of similar magnitude is applied along the σ axis (see section 5.2.4). The advection and adjustment time-steps used are $\Delta t_s = 1.2\, s$ and $\Delta t_a = 0.3\, s$. The elliptic equation is solved with SOR, using $rl = 1.9$ as relaxation factor and $\epsilon = 10^{-6}$ as criterion of convergence. About four iterations were required per adjustment time-step for the criterion of convergence to be met. The potential temperature perturbation $\theta^{'}$ fields from the isentropic background state after 360, 540, 720 and 900 s are shown in Fig. 5.22, for a vertical cross section along $y = 0$. The contour interval is 1 K. The corresponding vertical velocity fields $\hat{w}$ are shown in Fig. 5.24, with the contour interval 2 ms^{-1}. Note the displacement of the vertical scale in Fig. 5.22 relative to Fig. 5.24. The $\theta^{'}$ field at $\sigma = 1$ is displayed in Fig. 5.23, for t = 360, 540, 720 and 900 s.

Some remarks can be made from considering the results displayed in Figs. 5.22 to 5.24:

- the intensity of the potential temperature disturbance in the three-dimensional simulation is considerably less than in the two-dimensional simulations (compare Panel d of Fig. 5.22 to Panel d of Fig. 5.12). This may be related to the fact that there are physical differences between the two and three-dimensional cold bubble downburst problems. In the three-dimensional problem, the gust front spreads out into a three-dimensional environment after reaching the surface. This is probably the most important reason for the relatively less intene disturbance in the three-dimensional environment;

- the damping of the tri-cubic spatial interpolation scheme may also contribute to the relatively smaller amplitude of the disturbance in the three-dimensional simulation;

- after the cold bubble reaches the surface in the three-dimensional simulation, it spreads out radially as a gust front (Fig. 5.23). The gust front progresses more slowly away from the center of the domain than in the corresponding two-dimensional simulation. By t = 900 s, the leading edge of the gust front is about 11 km away from its orgin in the plane $\sigma = 0$, compared to the about 14 km it travels in the two dimensional simulations (compare Panels d of Figs. 5.22 and 5.12). The relatively slower progress of the gust front in the three-dimensional simulation may be related to the lower intensity of the disturbance, that loses its momentum more rapidly as it spreads out into the three-dimensional environment;

- one Kelvin-Helmholtz instability rotor is simulated to develop along the leading edge of the gust front as it spreads out radially (Fig. 5.26). The corresponding two-dimensional simulation is similar in this respect, showing a second rotor that is starting to develop at t = 900 s (Panel d of Fig. 5.13) . The intensity of the rotor is less in the three-dimensional case, however;
- the three-dimensional simulations are smooth and without any signs of numerical noise;
- It may be said that the split semi-Lagrangian scheme provides a satisfactorily solution of the three-dimensional cold bubble downburst problem.

5.5 A warm bubble experiment in three spatial dimensions

5.5.1 Design of the three-dimensional warm bubble test

The experiment described in this section is an extension of the two-dimensional warm bubble test described in section 5.3.1 to three spatial dimensions. In an initially dry, at rest and isentropic atmosphere with potential temperature 300 K, a circularly-shaped initial disturbance is introduced for the potential temperature:

$$\Delta\theta_0(x,z) = 6.6\cos^2(\frac{\pi}{2}r), \tag{5.8}$$

for $r \leq 1$, where $r^2 = [(x-x_c)/x_t]^2 + [(y-y_c)/y]^2 + [(z-z_c)/z_t]^2$, $x_c = y_c = 0$ m, $z_c = 2750$ m, $x_t = y_t = 2500$ m and $z_t = 2500$ m.

The integration domain extends over $-10000\,m \leq x \leq 10000\,m$ and $-10000\,m \leq y \leq 10000\,m$ in the horizontal. The top of the model domain is chosen to be 135 hPa (about 13500 m). The center of the initial disturbance is in the middle of the horizontal domain, that is, 10 km away from any of the lateral boundaries. The horizontal resolution used is 500 m and 135 equally spaced σ levels are used to give a vertical resolution of about 100 m on the average. The experiment corresponds to the two-dimensional warm bubble experiment WPM described in section 5.3.3, that was performed at similar horizontal and vertical resolutions.

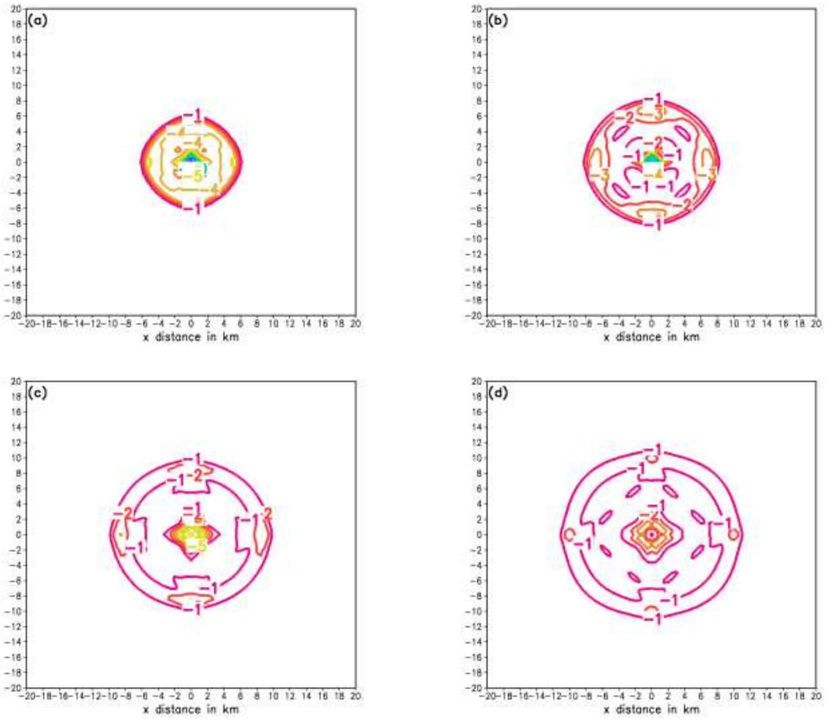

Figure 5.23: The three-dimensional cold bubble test. Horizontal cross section of the potential temperature perturbation at $\sigma = 0$, for : (a) after 360 s; (b) after 520 s; (c) after 720 s; (d) after 900 s. The full horizontal domain $-20000\,m \leq x \leq 20000\,m$, $-20000\,m \leq y \leq 20000\,m$ is shown. The contour interval is 1 K.

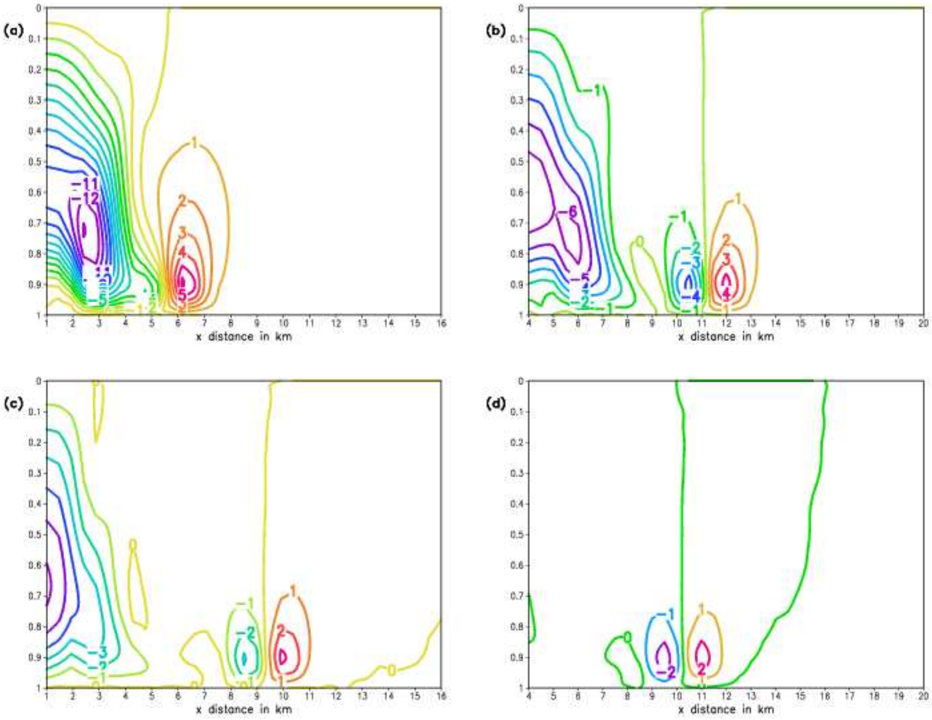

Figure 5.24: The three-dimensional cold bubble test. Vertical cross section of the vertical velocity $\hat{w}$ field at $y = 0$, for $0 \leq \sigma \leq 1$: (a) after 360 s; (b) after 520 s; (c) after 720 s; (d) after 900 s. The contour interval is 1 ms^{-1}. Note the displacement of the horizontal scale in (d).

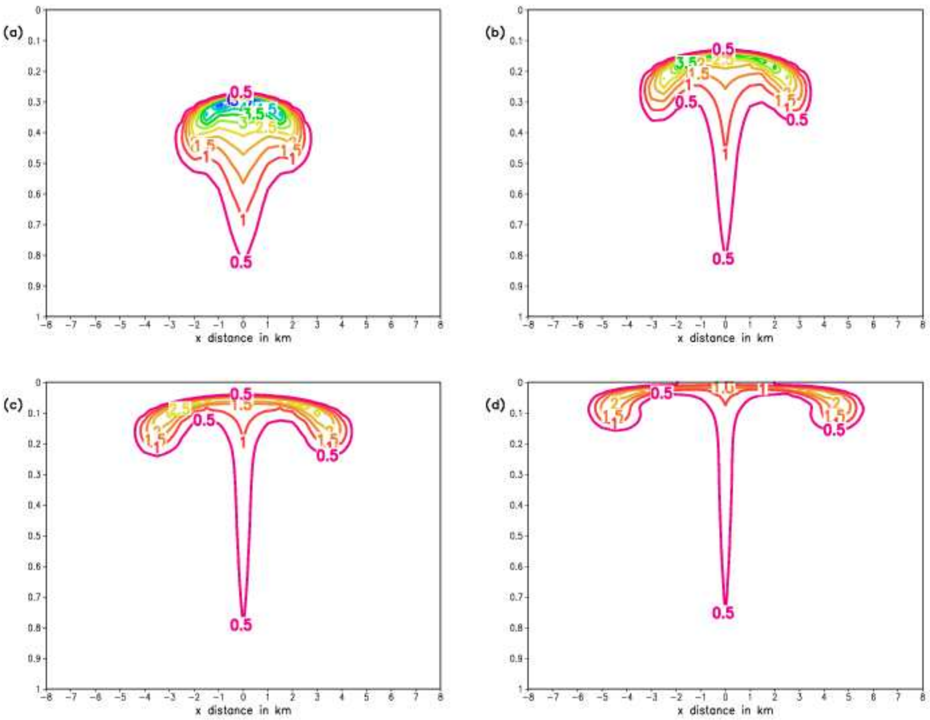

Figure 5.25: The warm bubble test in three spatial dimensions. Vertical cross section of the potential temperature perturbation at $y = 0$, for $-8000\,m \leq x \leq 8000\,m$ and $0 \leq \sigma \leq 1$: (a) after 360 s; (b) after 520 s; (c) after 720 s; (d) after 900 s. The contour interval is 0.5 K.

5.5.2 A three-dimensional warm bubble simulation obtained with fourth order differencing

The numerical settings used to obtain the three-dimensional warm bubble simulation in the present section, are as described for the three dimensional cold bubble test (see section 5.4.2). The only difference are with respect to the values of diffusion coefficients used. The same settings of explicit diffusion were used to obtain the corresponding two-dimensional warm bubble simulation WPM described in section 5.3.3. That is, $K_s = 300\,m^2s^{-1}$ and $K_{Ts} = 50\,m^2s^{-1}$, with diffusion of similar magnitudes applied along the σ axis, for u and T respectively. The elliptic equation is solved with SOR, using $rl = 1.6$ as relaxation factor and $\epsilon = 10^{-6}$ as criterion of convergence. On average only one iteration was required per adjustment time-step for the criterion of convergence to be met. The potential temperature deviation $\theta^{'}$ from the isentropic background state after 360, 540, 720 and 900 s is shown in Fig. 5.25, for a vertical cross section along $y = 0\,m$. The contour interval is 0.5 K. The corresponding vertical velocity fields $\hat{w}$ are shown in Fig. 5.26, with contour interval 2ms^{-1}.

A few remarks can be made with regard to the simulation displayed in Figs. 5.25 and 5.26:

- generally, the time evolution of the flow features in the three-dimensional simulation are very similar to that of the two-dimensional reference solution (see section 5.3.2). In particular, the development of the rotors on both sides of the symmetry axis are simulated (Fig. 5.26). The rotors entrain relatively cooler air from the environment into the lower part of the bubble (note the intrusion of the 0 K contour into the lower part of the bubble in Panels b to c of Fig. 5.25), whilst divergent motion caused by the rotors result in the formation of potential temperature maxima on both sides of the center axis (Panels b to c of Fig. 5.25);

- the rate of ascent of the three-dimensional warm bubble corresponds closely to that of the two-dimensional bubble in the reference solution (compare Fig. 5.25 to Fig. 5.16);

- however, the lateral displacement of the disturbance by t = 900 s (Panel d of Fig. 5.25) is somewhat less than that of the two-dimensional reference solution (Panel d of Fig. 5.16) and the two-dimensional simulation WPM (Panel d of Fig. 5.18) performed at similar resolutions than the present experiment. A similar result was obtained with regard to the displacement of the gust front in the three-dimensional cold bubble test (see the previous section);

- the potential temperature perturbation in the three-dimensional simulation is less intense than the reference two-dimensional simulation at t = 900 s ($\theta^{'}_{max} = 2.15\,K$ for the three-dimensional simulation compared to $\theta^{'}_{max} = 4.24\,K$ for the two-dimensional case). The relative stronger damping of the three- dimensional solution may be related to the explicit diffusion that takes place as the bubble spreads out into the three-dimensional environment. The damping of the tri-cubic interpolation scheme may also contribute to the relatively smaller amplitude of the $\theta^{'}$ (and $\hat{w}$) field of the three-dimensional solution;

- the vertical velocity field at t = 900 s (Panel) is similar to that of the corresponding two-dimensional simulation (Panel d of). However, the downdrafts in particular are less intense in the case of the three-dimensional solution. Two secondary updrafts are starting to develop in the three-dimensional solution at t = 900 s;

- in totality, it may be said that the split semi-Lagrangian scheme gives a satisfactorily solution of the warm bubble test in three spatial dimensions.

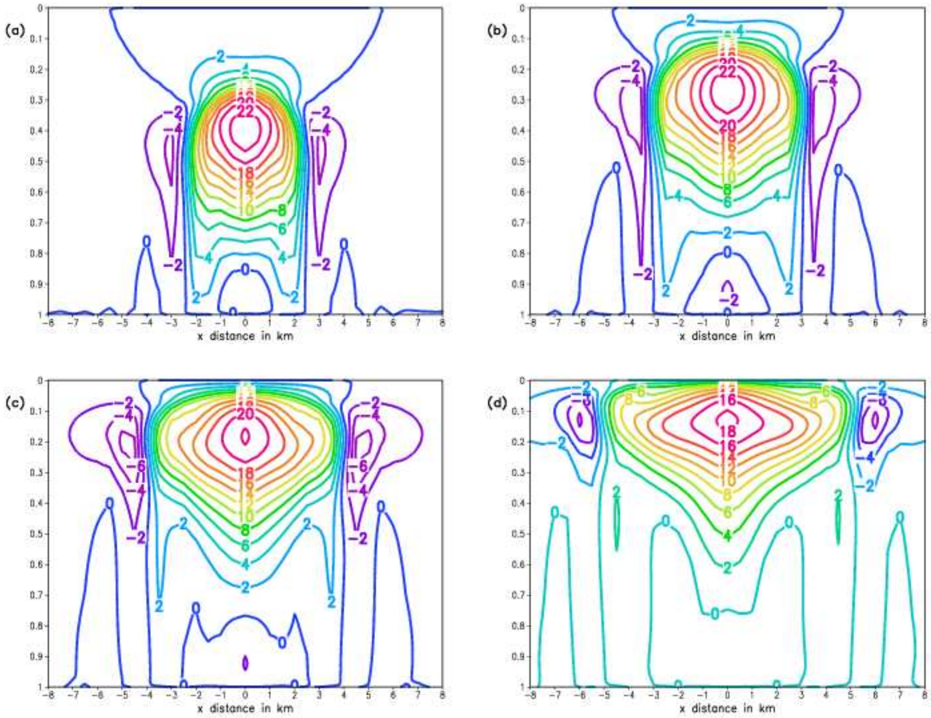

Figure 5.26: The warm bubble test in three spatial dimensions. Vertical cross section of the vertical velocity $\hat{w}$ at $y = 0$, for $-8000\,m \leq x \leq 8000\,m$ and $0 \leq \sigma \leq 1$: (a) after 360 s; (b) after 520 s; (c) after 720 s; (d) after 900 s. The contour interval is 2 ms^{-1}.

5.6 A three-dimensional warm bubble in an environment with strong unidirectional wind shear

5.6.1 Design of the experiment

In this experiment a warm bubble is introduced to an atmosphere with strong unidirectional vertical wind shear. The initial environment is dry and isentropic, and in hydrostatic balance. The x component of the initial horizontal wind has vertical shear of

$$\frac{d\tilde{u}}{dz} = 0.005\,s^{-1}, \tag{5.9}$$

that is, the x component of the horizontal wind increases with $20\,ms^{-1}$ over each interval of $4000\,m$ in the vertical. The initial y component of the horizontal wind and the vertical motion field are zero.

The integration domain is larger than in the previous experiment, and extends over $0\,m \leq x \leq 50\,000\,m$ and $0\,m \leq y \leq 50\,000\,m$ in the horizontal. The top of the model domain is chosen to be 135 hPa (about 13500 m) as before. The shape and intensity of the initial disturbance in the potential temperature is given by (5.8), with $x_c = 10\,000\,m$, $y_c = 25\,000\,m$, $z_c = 2750\,m$ and $x_t = y_t = z_t = 2500\,m$. In its initial position, the center of the bubble is located $10\,000\,m$ away from the upstream boundary $x = 0\,m$. The horizontal resolution used is $1000\,m$, and 135 equally spaced σ levels are used to give a vertical resolution of about $100\,m$ on the average.

The model was initialized following the procedure described in section 5.2.2. The boundary conditions are as described in section 4.9, with the exception of the lateral boundary conditions that are imposed on u. During the integration, the latter is kept constant at its initial vertical profile determined by (5.9) at all the lateral boundaries. The numerical settings of the split semi-Lagrangian scheme are as in section 5.5. The advection and adjustment time-steps used are $\Delta t_s = 1.2\,s$, $\Delta t_a = 0.3\,s$ and the integration period is $900\,s$. One average only one iteration of the SOR procedure was needed per adjustment time-step for the criterion of convergence to be met.

5.6.2 Horizontal splitting of the disturbance in the environment with vertical wind shear

The potential temperature perturbation $\theta^{'}$ from the isentropic background state after 360, 540, 720 and 900 s are shown in Fig. 5.27, for a vertical cross section along $y = 25\,000\,m$. The contour interval is $0.5\,K$. The corresponding vertical velocity fields $\hat{w}$ are shown in Fig. 5.28, with the contour interval $1\,ms^{-1}$. Horizontal cross sections of $\theta^{'}$ at levels of constant σ are shown in in Fig. 5.29, for $t = 360$, 540, 720 and $900\,s$. The contour interval is $0.5\,K$. The constant

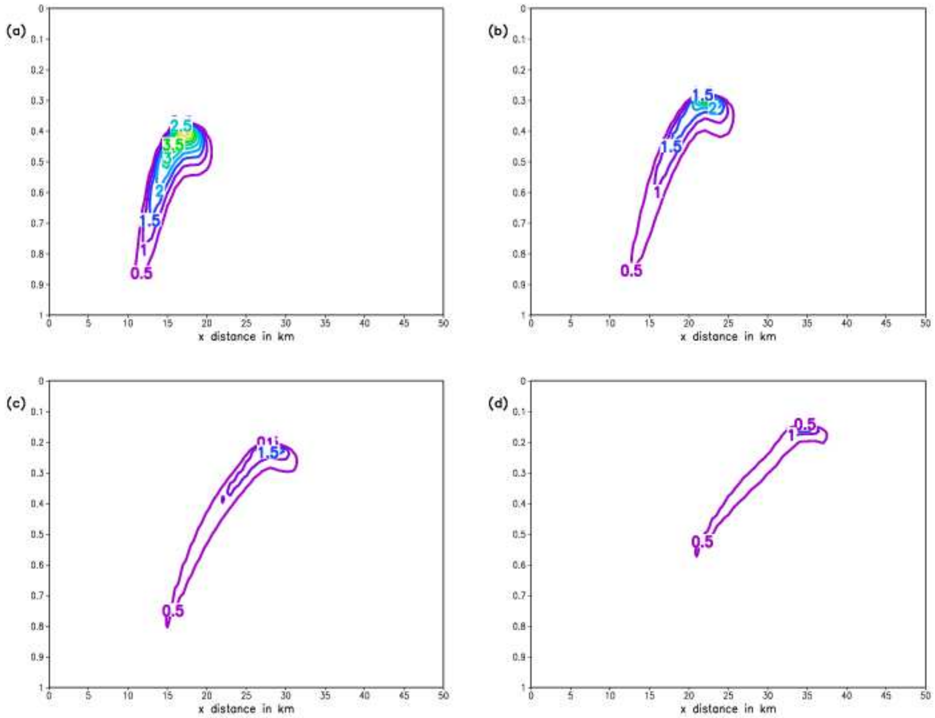

Figure 5.27: The three-dimensional warm bubble in an environment with strong unidirectional vertical wind shear. Vertical cross section of the potential temperature perturbation at $y = 25\,000\,m$ and $0 \leq \sigma \leq 1$: (a) after $360\,s$; (b) after $540\,s$; (c) after $720\,s$; (d) after $900\,s$. The contour interval is $0.5\,K$.

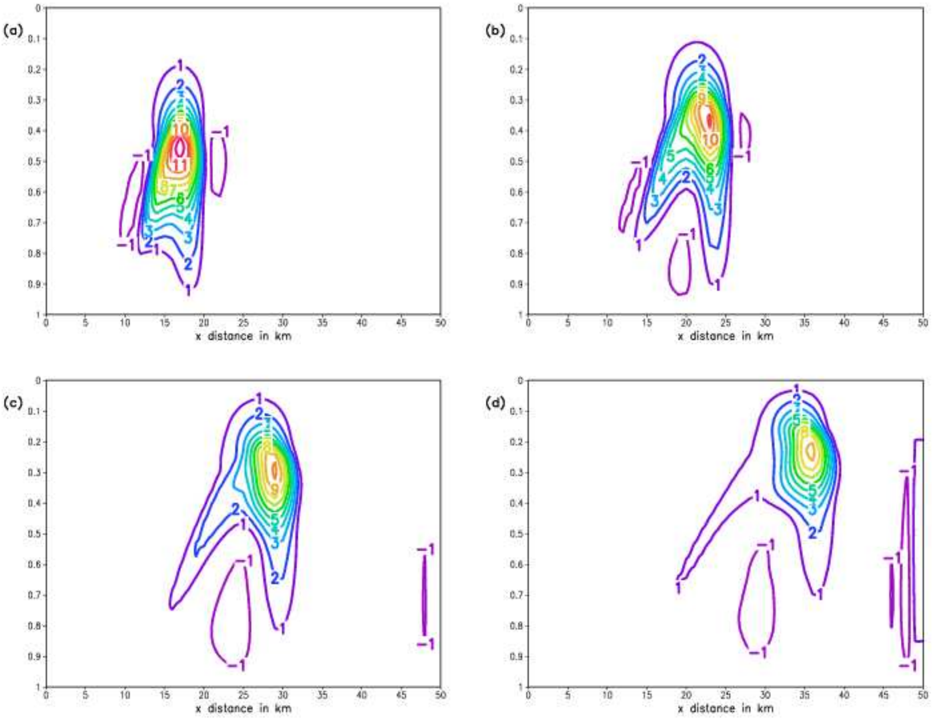

Figure 5.28: The three-dimensional warm bubble in an environment with strong unidirectional vertical wind shear. Vertical cross section of the vertical component of the wind $\hat{w}$ at $y = 25\,000\,m$ and $0 \leq \sigma \leq 1$: (a) after $360\,s$; (b) after $540\,s$; (c) after $720\,s$; (d) after $900\,s$. The contour interval is $1\,ms^{-1}$.

sigma levels are 0.44, 0.37, 0.29 and 0.22 for Panels a to d, respectively. For each of the time-levels, the σ level used corresponds to the height at which the vertical velocity attains a maximum along $y = 25\,000\,m$. Note the displacement of the horizontal scale in Panels a to d of Fig. 5.29.

In Fig. 5.27 it can be seen how the warm bubble rises in the environment with strong vertical wind shear, while being advected in the positive x direction by the u component of the wind. Because of the increase in the magnitude of u with height, the horizontal displacement of the upper part of the bubble is the fastest. Initially, the updraft induced by the positive buoyancy of the bubble is tilted slightly in the positive x direction by the horizontal wind field (Panel a of Fig. 5.28). Rotors develop along the outermost edges of the bubble (note the downdrafts in Panels a and b of Fig. 5.28). These rotors are even better developed along the flanks of the bubble that are perpendicular to the advecting wind u (not shown). As time goes by, the orientation of the core of the updraft gradually changes its orientation and eventually it is tilted in the negative x

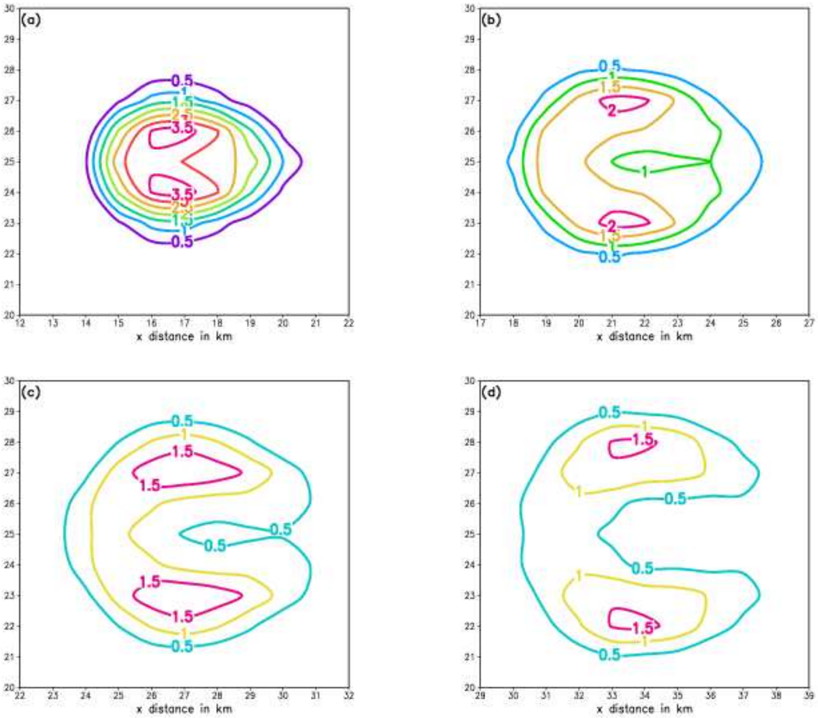

Figure 5.29: The three-dimensional warm bubble in an environment with strong unidirectional vertical wind shear. Horizontal cross section of the potential temperature perturbation for: (a) after $360\,s$ at $\sigma = 0.44$; (b) after $540\,s$ at $\sigma = 0.37$; (c) after $720\,s$ at $\sigma = 0.29$; (d) after $900\,s$ at $\sigma = 0.22$. The contour interval is $0.5\,K$. The σ level used for each time-step correspond to the height of maximum vertical velocity along $y = 25\,000\,m$. Note that $20\,000\,m \leq y \leq 30\,000\,m$, with a displacement of the x direction scale in the Panels.

direction (Fig. 5.28 Panels c and d).

Figure 5.29 shows how the potential temperature perturbation maximum on the σ level that corresponds to the height of maximum vertical velocity, splits around the vertical center axis of the bubble during its displacement in the positive x direction by the horizontal wind. Two potential temperature maxima, one on each side of the vertical center axis, are well developed by $t = 900\,s$. The "horizontal splitting" of the potential temperature disturbance is indicative of a feature that is well-known from the linear theory of rotating thunderstorms, namely "storm splitting" (e.g. Klemp, 1987; Holton, 1992). In an environment characterized by strong unidirectional vertical wind shear, low pressure areas develop on both the left and right flanks of the original updraft (Klemp, 1987). These tend to be the strongest at the middle levels of the atmosphere. The associated pressure forcing may be sufficient to cause the updraft to split into two separate updrafts moving to the right and left of the environmental wind. The left- and right-moving updrafts rotate clockwise and anticlockwise, respectively. The rotation that develops is the result of the tilting of horizontal shear vorticity into the vertical by the original updraft (e.g. Rotunnu, 1981; Davies-Jones, 1983; Holton, 1992). Storm splitting has indeed been observed for cases where strong unidirectional wind shear has been observed in the real atmosphere (Fujita and Grandoso, 1968).

Figure 5.30 shows the vertical velocity $\hat{w}$ (shaded) and the vertical component of the vorticity $\zeta = \partial v/\partial x - \partial u/\partial y$ (contours) at $t = 900\,s$, for a portion of the horizontal domain at $\sigma = 0.48$. Indeed, negative vorticity (indicating clockwise rotation) and positive vorticity (indicating anticlockwise rotation) are present to the left and right of the center axis $y = 25\,000\,m$, respectively. The development of the potential temperature maxima on each side of this center axis (Fig. 5.29) may be attributed to advection that results from the two counterrotating vortices. Two well established updrafts can also be seen at $t = 900\,s$ (Fig. 5.30), moving to the left and right of the environmental wind. It is interesting to note that the splitting of the original updraft into the two separate updrafts is best developed well below the region of maximum vertical velocity at $\sigma = 0.22$ (Panel d of Fig. 5.28), where a single updraft still exists by $t = 900\,s$.

The results described in this section correspond very well to the linear theory of storm splitting and the development of rotation in thunderstorms. Clearly, the new model kernel based on a split semi-Lagrangian formulation of the quasi-elastic equations can be used to adequately describe highly nonlinear and non-hydrostatic flow. A detailed study of the dynamics relevant to the present experiment falls beyond the scope of the thesis, but the experiment illustrates the potential of the new model to be used in the study of nonhydrostatic circulation systems.

5.7 Discussion

In this chapter the split semi-Lagrange formulation of the quasi-elastic equations has been applied to simulate bubble convection in two and three spatial dimensions. For the two-dimensional tests the available computing power allowed high-resolution simulations, where the flow is adequately resolved, to be performed. For the three-dimensional tests, the flow features are marginally resolved. The three-dimensional convective bubbble experiments performed appear to be of the first to be described in literature. A new test where a warm bubble ascends in an environment with strong unidirectional wind shear was devised. Overall, the results obtained in this section confirms that the both the two- and three-dimensional split semi-Lagrangian formulations of the quasi-elastic equations are robust, and may be used to describe highly nonlinear and nonhydrostatic flow.

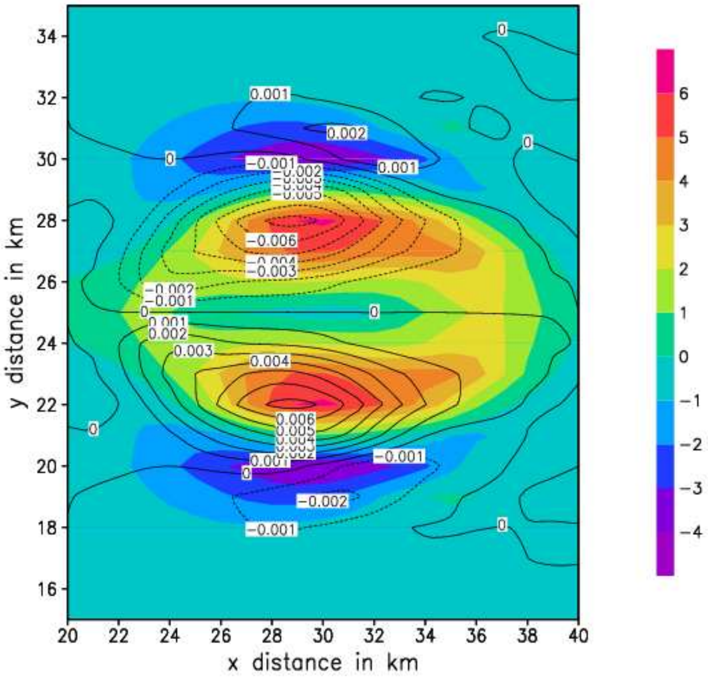

Figure 5.30: The vertical component of the wind $\hat{w}$ (shaded, ms^{-1}) and the vertical component of the vorticity ζ (contours, s^{-1}) at $\sigma = 0.48$ and $t = 900\,s$.

With regard to the properties and performance of the split semi-Lagrangian scheme, the most important results may be summarized as follows:

- no advantage was found in going beyond the D_2 scheme of McGregor (1993) for the calculation of departure points;
- fourth order differencing of the adjustment step equations provides superior results compared to second order differencing. In particular, the gravity wave phase speed is less retarded when fourth order differencing is used, which results in more accurate simulations of the time-evolution of the main flow features;
- explicit diffusion and the damping applied by the bicubic interpolation scheme at the shortest resolvable scales are often sufficient to control the development of two-grid interval noise on the nonstaggered grid, in particular when the flow is marginally resolved (as in the three-dimensional tests);
- however, for high-resolution tests where the flow is adequately resolved, it is essential that the Shapiro spatial filter is applied. The filter effectively removes the two-grid-interval waves, and two-grid-interval noise, from the nonstaggered grid. The filter suppresses the development of nonlinear instability at the shortest resolvable scales, allowing in particular a larger advection time-step to be used in the simulations;
- for adequately resolved flow, the split semi-Lagrangian scheme produces accurate results that are comparable to those obtained with high order finite element and fine difference models;
- for marginally resolved flow (in two and three spatial dimensions), the solutions obtained are damped, but smooth, stable and useable;
- a unique property of the split semi-Lagrangian scheme is that it performs well for both the cases of adequately and marginally resolved flow. Damped advection schemes generally perform well when the flow is marginally resolved, but spuriosly retard the time-evolution of flow features when the flow is adequatly resolved. High order finite element and finite difference models generally gives accurate results when the flow is adequately resolved, but produce noisy solutions for marginally resolved flow. The reason for the satisfactorily solutions produced by the split semi-Lagrangian scheme for both the cases of adequately and marginally resolved flow is to be found in its dual nature: the advection process may be treated during the advection step, whilst the fast travelling gravity waves may be treated accurately by using a smaller adjustment time-step.
- At high spatial resolutions, both the semi-implicit and explicit schemes require the use of small time-steps, for accuracy and stability reasons, respectively. Here the split semi-Lagrangian scheme may offer a computational advantage over other schemes, since it may be applied with a

relatively large advection time-step. The fast travelling waves may still be treated accurately by using a small adjustment time-step.

- The SOR procedure provides reasonably efficient solutions of the elliptic equation, in both two and three spatial dimensions.

It is appealing from a computational perspective to use a nonstaggered grid when using a semi-Lagrangian approach for the simulation of advection, since only one set of trajectories needs to be calculated. On the other hand, the damping at the shortest resolvable scales by the bicubic interpolation scheme used in the semi-Lagrangian scheme described here contributes to control the two-grid interval noise that may develop on the nonstaggered grid. It may therefore be said that when discretizing the atmospheric equations on a nonstaggered grid, it is appealing to use a semi-Lagrangian approach, rather than an Eulerian procedure, to discretize the advection terms.

It may be noted that all the bubble convection tests performed in this Chapter are carried out in an isentropic environment, that is, the environment is neutrally stratified. This effectively filters out internal gravity waves, which develop in a stably stratified environment, from the numerical solutions. The experiments may be extended to stably stratified environments, in order to investigate the performance of the split semi-Lagrangian scheme under these conditions. However, since the fastest travelling waves in the equation system are the Lamb waves (Miller and White, 1984; also see Chapter 3), internal gravity waves are not likely to have a dominant effect on the maximum size of the adjustment time step allowed. Preliminary tests of airflow over a three-dimensional bell-shaped mountain in a stably stratified environment (not shown) have been performed with the split semi-Lagrangian scheme, at a horizontal resolution of 500 m and a vertical resolution of about 100 m. The scheme was found to be stable at large advection Courant numbers, and at adjustment time-steps of size similar to those used in the convective bubble tests.

The emphasis in this Chapter is on the simulation of micro- and meso-scale buoyance driven flows, where the Coriolis effect is of negligible importance. The dynamic kernel has not been tested at the synoptic-scale, where the geostrophic adjustment process occurs. Of particular interest would be how the semi-implicit treatment of the Coriolis terms (see section 4.5.2) impact on numerical stability during the adjustment phase of the solution procedure. Purser and Leslie (1988) have shown that for the system of gravity-inertia wave equations (e.g. Mesinger and Arakawa, 1976), geostrophic adjustment on the nonstaggered grid may be treated accurately using high order spatial differencing and filtering. They've extended this approach to a hydrostatic primitive equation model (Leslie and Purser, 1991). These results provide some confidence that the split semi-Lagrangian formulation of the quasi-elastic equations will perform well, at least from a numerical perspective, at spatial scales larger than the meso-scale.

All the simulations in this chapter were performed on a personal computer (PC). Computational constraints prevented the three-dimensional simulations to be performed at spatial resolutions where the flow is adequately resolved. Recently, a PC cluster was obtained by the Faculty of Science at the University of Pretoria. This makes possible more extensive testing of the performance of the scheme in three spatial dimensions in the future.